1 Chemical characteristics and causes of airborne particulate pollution in warm

2 seasons in Wuhan, central China

4 X.P. Lyu [1], N. Chen [2], H. Guo [1*], L.W. Zeng [1], W.H. Zhang [3], F. Shen [2], J.H. Quan [2], N. Wang [4]

5 [1] Department of Civil and Environmental Engineering, The Hong Kong Polytechnic University,

6 Hong Kong

7 [2] Hubei Provincial Environment Monitoring Center, Wuhan, China

8 3 Department of Environmental Sciences, School of Resource and Environmental Sciences,

9 Wuhan University, Wuhan, China

10 4 Guangdong Provincial Key Laboratory of Regional Numerical Weather Prediction, Institute of

11 Tropical and Marine Meteorology, Guangzhou, China

12 *Corresponding author. Tel: +852 3400 3962; Fax: +852 2334 6389; Email:

13 ceguohai@polyu.edu.hk

15 **Abstract:** Continuous measurements of airborne particles and their chemical compositions were

16 conducted in May, June, October, and November 2014 at an urban site in Wuhan, central China.

17 The results indicate that particle concentrations remained at a relatively high level in Wuhan,

18 with averages of 135.1 $\pm$ 4.4 (mean $\pm$ 95% confidence interval) and 118.9 $\pm$ 3.7 $\mu g/m^3$ for PM_{10}

19 and 81.2 $\pm$ 2.6 and 85.3 $\pm$ 2.6 $\mu g/m^3$ for $PM_{2.5}$ in summer and autumn, respectively. Moreover,

20 $PM_{2.5}$ levels frequently exceeded the National Standard Level II (i.e., daily average of 75 $\mu g/m^3$),

21 and six $PM_{2.5}$ episodes (i.e., daily $PM_{2.5}$ averages above 75 $\mu g/m^3$ for 3 or more consecutive days)

22 were captured during the sampling campaign. Potassium was the most abundant element in $PM_{2.5}$,

23 with an average concentration of 2060.7 $\pm$ 82.3 ng/m^3; this finding indicates intensive biomass

24 burning in and around Wuhan during the study period, because almost no correlation was found

25 between potassium and mineral elements (iron and calcium). The source apportionment results

26 confirm that biomass burning was the main cause of episodes 1, 3, and 4, with contributions to

27 $PM_{2.5}$ of 46.6% $\pm$ 3.0%, 50.8% $\pm$ 1.2%, and 44.8% $\pm$ 2.6%, respectively, whereas fugitive dust

28 was the leading factor in episode 2. Episodes 5 and 6 resulted mainly from increases in vehicular

29 emissions and secondary inorganic aerosols, and the mass and proportion of NO_3^- both peaked

30 during episode 6. The high levels of NO_x and NH_3 and the low temperature during episode 6

31 were responsible for the increase of NO_3^-. Moreover, the formation of secondary organic carbon

32 was found to be dominated by aromatics and isoprene in autumn, and the contribution of
33 aromatics to secondary organic carbon increased during the episodes.

34 **Keywords:** $PM_{2.5}$; NO_3^-; SOA; biomass burning; formation mechanism

1. Introduction

37 Airborne particulate pollution, also called "haze," has swept across China in recent years,
38 particularly over its northern, central, and eastern parts (Cheng et al., 2014; Kang et al., 2013;
39 Wang et al., 2013). Due to its detrimental effects on human health (Anderson et al., 2012;
40 Goldberg et al., 2001), the atmosphere (Yang et al., 2012; White and Roberts, 1977), acid
41 precipitation (Zhang et al., 2007; Kerminen et al., 2001), and climate change (Ramanathan et al.,
42 2001; Nemesure et al., 1995), particulate pollution has become a major concern of scientific
43 communities and local governments. China's national ambient air quality standards issued in
44 2012 regulate the annual upper limit of PM_{10} (i.e., particulate matter with an aerodynamic
45 diameter of less than 10 μm) and $PM_{2.5}$ (i.e., particulate matter with an aerodynamic diameter of
46 less than 2.5 μm) as 70 μg/m^3 and 35 μg/m^3 and 24-h averages as 150 μg/m^3 and 75 μg/m^3,
47 respectively (GB 3095-2012).

48 Numerous studies have been conducted in China to understand the spatiotemporal variations in
49 particle concentrations, the chemical composition, and the causes of haze events (Cheng et al.,
50 2014; Cao et al., 2012; Zheng et al., 2005; Yao et al., 2002). In general, particulate pollution is
51 more severe in winter due to additional emissions (e.g., coal burning) and unfavorable dispersion
52 conditions (Lyu et al., 2015a; Zheng et al., 2005). Northern China often suffers heavier, longer,
53 and more frequent haze pollution than southern China (Cao et al., 2012). Chemical analysis
54 indicates that secondary inorganic aerosol (SIA; i.e., sulfate [SO_4^{2-}], nitrate [NO_3^-], and
55 ammonium [NH_4^+]) and secondary organic aerosol (SOA) dominate the total mass of airborne
56 particles (Zhang et al., 2014; Zhang et al., 2012). However, the composition differs among the
57 size-segregated particles. In general, secondary species and mineral or sea salt components are
58 prone to be apportioned in fine and coarse particles (Zhang et al., 2013; Theodosi et al., 2011).
59 Indeed, the general characteristics of particles (e.g., toxicity, radiative forcing, acidity) are all
60 tightly associated with their chemical compositions and physical sizes, which therefore have
61 been extensively studied in the field of aerosols. To better understand and control airborne
62 particulate pollution, the causes and formation mechanisms have often been investigated (Wang

63 et al., 2014a and b; Kang et al., 2013; Oanh and Leelasakultum, 2011). Apart from the

64 unfavorable meteorological conditions, emission enhancement was often the major culprit. There

65 is little doubt that industrial and vehicular emissions contributed greatly to the particle mass via

66 direct emission and secondary formation of particles from gaseous precursors, such as sulfur

67 dioxide (SO_2), nitrogen oxides (NO_x), and volatile organic compounds (VOCs; Guo et al., 2011a).

68 In addition, some other sources in specific regions or during specific time periods have also built

69 up the particle concentrations to a remarkable degree, e.g., coal combustion in north China (Cao

70 et al., 2005; Zheng et al., 2005) and biomass burning in Southeast Asia (Deng et al., 2008; Koe et

71 al., 2001). Furthermore, some studies have explored the possible formation mechanisms of the

72 main particle components (SIA and SOA) and distinguished the contributions of different

73 formation pathways. For example, Wang et al. (2014) demonstrated that heterogeneous oxidation

74 of SO_2 on aerosol surfaces was an important supplementary pathway to particle-bound SO_4^{2-} in

75 addition to gas phase oxidation and reactions in clouds. In contrast, it was reported that

76 homogeneous and heterogeneous reactions dominated the formation of NO_3^- during the day and

77 night, respectively (Pathak et al., 2011; Lin et al., 2007; Seinfeld and Pandis, 1998). Furthermore,

78 biogenic VOCs and aromatics were shown to be the main precursors of SOA (Kanakidou et al.,

79 2005; Forstner et al., 1997).

80 Despite numerous studies, the full components of airborne particles have seldom been reported

81 due to the cost of sampling and chemical analysis, resulting in a gap in our understanding of the

82 chemical characteristics of particles. In addition, although the causes of particle episodes have

83 been discussed in many case studies (Wang et al., 2014; Deng et al., 2008), the contributions

84 have rarely been quantified. Furthermore, the formation mechanisms might differ in various

85 circumstances. Therefore, an overall understanding of the chemical characteristics of airborne

86 particles, the causes of the particle episodes, and the formation mechanisms of the enhanced

87 species would be of great value. In addition, the frequent occurrence of haze pollution has

88 become a regular phenomenon in central China during warm seasons, but the causes have not

89 been identified and the contributions have not been quantified. Wuhan is the largest megacity in

90 central China and has suffered from severe particulate pollution in recent years. The data indicate

91 that the frequency of days in which $PM_{2.5}$ exceeded the national standard level II (i.e., a daily

92 average of 75 μg/m^3) in Wuhan reached 55.1% in 2014 (Wuhan Environmental Bulletin, 2014).

93 In the warm seasons of 2014, the hourly maximum $PM_{2.5}$ (564 μg/m^3) was even higher than that

94 in winter (383 µg/m^3), as shown in Figure S1 in the Supplementary Material. Moreover, because

95 the air quality in Wuhan is strongly influenced by the surrounding cities, the pollution level in

96 Wuhan also reflects the status of the city clusters in central China. However, previous studies

97 (Lyu et al., 2015a; Cheng et al., 2014) did not allow a complete understanding of the properties

98 of airborne particles in this region, particularly during the warm seasons, nor could they guide

99 control strategies. It is therefore urgent to understand the chemical characteristics of airborne

100 particles and to explore the causes and formation mechanisms of the particle episodes in Wuhan.

101 This study comprehensively analyzed the chemical characteristics of PM$_{2.5}$ in Wuhan from a full

102 suite of component measurement data: SO$_4^{2-}$, NO$_3^-$, NH$_4^+$, organic carbon (OC), including

103 primary organic carbon (POC) and secondary organic carbon (SOC), elemental carbon (EC), and

104 elements. Furthermore, based on the analysis of meteorological conditions, chemical signatures,

105 source apportionment, and distribution of wildfires, the causes of the PM$_{2.5}$ episodes are

106 identified and their contributions quantified. Finally, this study used a photochemical box model

107 incorporating a master chemical mechanism (PBM-MCM) and theoretical calculation to

108 investigate the formation processes of NO$_3^-$ and SOC. Ours is the first study to quantify the

109 contribution of biomass burning to PM$_{2.5}$ and examine the formation mechanisms of both

110 inorganic and organic components in PM$_{2.5}$ in central China.

111

112 **2. Methods**

113 **2.1 Data collection**

114 The whole set of air pollutants were continuously monitored at an urban site in the largest

115 megacity of central China, i.e., Wuhan. The measurement covered two periods: May and June in

116 summer and October and November in autumn of 2014. The measured species included particle-

117 phase pollutants such as PM$_{10}$, PM$_{2.5}$, and particle-bound components and gas-phase pollutants,

118 including VOCs, SO$_2$, CO, NO, NO$_2$, O$_3$, HNO$_3$ (g), NH$_3$ (g), and HCl (g). Hourly data were

119 obtained for each species. The sampling site (30.54 °N, 114.37 °E) was located in the Hubei

120 Environmental Monitoring Center Station, as shown in Figure 1, located in a mixed commercial

121 and residential area in which industries are seldom permitted. The instruments were housed in a

122 room in a six-story building (~18 m above ground level) adjacent to a main road at a straight-line

123 distance of ~15 m. The traffic volume of the road was around 200 vehicles per hour. However, a

124 wall (~2 m high) and several rows of trees (7 to 8 m high) were located between the road and the

125   sampling site.

126   PM_{10} and $PM_{2.5}$ were measured with a continuous ambient particulate monitor (Thermo Fisher-

127   1405D, USA) integrated with a filter dynamics measurement system to minimize the loss of

128   semivolatile particulate matter. The water-soluble ions (WSIs) in $PM_{2.5}$ and gases including

129   HNO_3, HCl, and NH_3 were detected with an online ion chromatography monitor (Metrohm-

130   MARGA 1S, Switzerland). However, data were not available in May and June, because the

131   instrument was initially deployed in September. An aerosol OC/EC online analyzer (Sunset-RT-4,

132   USA); the NIOSH thermal-optical transmission method was used to resolve the carbonaceous

133   aerosols (OC and EC). In addition, the elements in $PM_{2.5}$ were measured with a customized

134   metal analyzer. This instrument used a $PM_{2.5}$ impactor to collect the airborne particulate samples,

135   which were analyzed by the β-ray in terms of mass concentrations. The filters loaded with

136   particles were then sent to an x-ray fluorescence analysis system for quantitative analysis. K^+

137   monitored by the online ion chromatography correlated well ($R^2 = 0.88$; slope = 0.80) with K

138   monitored by the customized metal analyzer. To keep consistency with other elements, K rather

139   than K^+ was used to do the following analyses in this study. For the analysis of trace gases (SO_2,

140   CO, NO, NO_2, and O_3), we used a suite of commercial analyzers developed by Thermo

141   Environmental Instruments Inc., which have been described in detail (Lyu et al. 2016; Geng et al.,

142   2009). Furthermore, a gas chromatography–flame ionization detector–mass spectrometry system

143   (TH_PKU-300) was used to resolve the real time data of the ambient VOCs. The details of the

144   analysis techniques, resolution, detection limits, and the protocol of quality assurance/control

145   were provided by Lyu et al. (2016) and Wang et al. (2014).

146
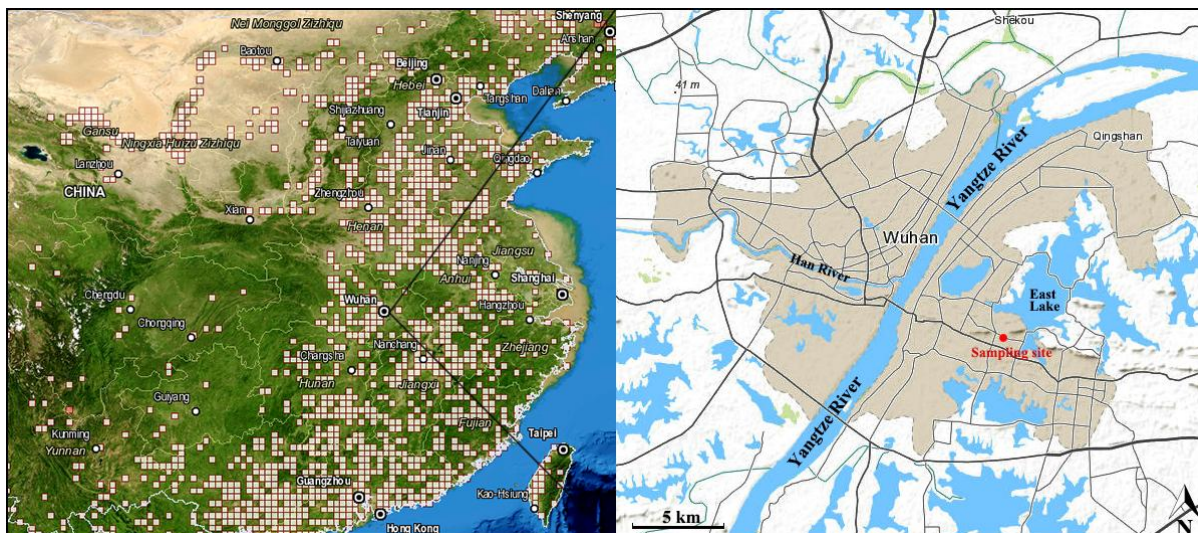
147

148 Figure 1. Geographic location of the sampling site. White blocks in left panel represent total

149 distribution of wildfires in autumn 2014, and urban area in Wuhan is highlighted in gray in the

150 right panel.

151

152 **2.2 Theoretical calculation and model simulation**

153 Theoretical calculation and model simulation were applied in this study to examine the formation

154 mechanisms of NO_3^- and SOC. The particle-bound NO_3^- was generally combined with NH_3 or

155 presented as HNO_3 in the ammonia-deficient environment, following the processes described in

156 R1 through R3 after HNO_3 was formed by the oxidation of NO_x (Pathak et al., 2011, Lin et al.,

157 2010). The production of NO_3^- can be calculated with Equations 1-4.

158 $NH_{3\,(g)} + HNO_{3\,(g)} \leftrightarrow NH_4NO_{3\,(s)}$ $k_1 = \exp\,[118.87 − 24084/T − 6.025\ln(T)]$ (ppb^2)   (R1)

159 $NH_{3\,(g)} + HNO_{3\,(g)} \leftrightarrow NH_4^+ + NO_3^-$ $k_2 = (P_1 − P_2\,(1 − a_w) + P_3\,(1 − a_w)^2) \times (1 − a_w)\,(1 −$

160 $a_w)^{1.75}k_1$ (ppb^2)   (R2)

161 $N_2O_5 + H_2O \rightarrow 2HNO_3$ $k_3 = \gamma/4(8kT/\pi m_{N2O5})0.5\,A_p$ (s^{-1})   (R3)

162 $\ln\,(P_1) = −135.94 + 8763/T + 19.12\ln\,(T)$ (Eq.1)

163 $\ln\,(P_2) = −122.65 + 9969/T + 16.22\ln\,(T)$ (Eq.2)

164 $\ln\,(P_3) = −182.61 + 13875/T + 24.46\ln\,(T)$ (Eq.3)

165 $[NO_3^-] = 0.775\left(\dfrac{[NH_3]+[HNO_3]-\sqrt{([NH_3]+[HNO_3])^2-4([NH_3][HNO_3]-k_1(k_2))}}{2}\right)$ (Eq.4)

166 where R1 and R2 describe the homogeneous formation of NO_3^- in humidity conditions lower

167 and higher than the deliquescence relative humidity of NH_4NO_3 (i.e., 62%; Tang and Munkelwitz,

168 1993), respectively. R3 presents the heterogeneous reaction of N_2O_5 on the preexisting aerosol

169 surfaces. k_{1-3} represents the rate of reactions R1-3. T, a_w, and P are the temperature, the relative

170 humidity, and the temperature-related coefficient, respectively. In R3, γ is the reaction

171 probability of N_2O_5 on aerosol surfaces, assigned as 0.05 and 0.035 on the surface of sulfate

172 ammonia and element carbon, respectively (Aumont et al., 1999; Hu and Abbatt, 1997). k is the

173 Boltzmann constant (1.38×10^{-23}), m_{N2O5} is the molecular mass of N_2O_5 (1.79×10^{-22} g), and A_p

174 is the aerosol specific surface area (cm^2/cm^3).

175 Furthermore, the PBM-MCM model was used to simulate the oxidation products in this study,

176 i.e., O_3, N_2O_5, the semi-volatile oxidation products of VOCs (SVOCs), and radicals such as OH,

177 HO_2, and RO_2. With full consideration of photochemical mechanisms and real meteorological

178 conditions, the model has been successfully applied in the study of photochemistry. Details about

179 the model construction and application were published by Lyu et al. (2015b), Ling et al. (2014),

180 and Lam et al. (2013).

181 **2.3 Source apportionment model**

182 The positive matrix factorization (PMF) model (EPA PMF v5.0) was used to resolve the sources

183 of PM$_{2.5}$. As a receptor model, PMF has been extensively used in the source apportionment of

184 airborne particles and VOCs (Brown et al., 2007; Lee et al., 1999). Detailed introductions of the

185 model can be found in Paatero (1997) and Paatero and Tapper (1994). Briefly, it decomposes the

186 input matrix (X) into matrices of factor contribution (G) and factor profile (F) in p sources, as

187 shown in Equation 5. The hourly concentrations of PM$_{2.5}$ components were included in the input

188 matrix. Values below the detection limit (DL; see Table S1 in the Supplement) were replaced

189 with DL/2. The uncertainties were $\sqrt{(10\% \times \text{concentration})^2 + \text{DL}^2}$ and 5/6×DL for the

190 samples with concentrations higher and lower than DL, respectively. The signal-to-noise (S/N)

191 ratios were all greater than 1, indicating "good" signal for all the species involved in source

192 apportionment, according to the PMF 5.0 User Guide. Samples with any missing values were

193 excluded. In total, 807 and 806 samples were applied for source apportionment in summer and

194 autumn, respectively.

195 The selection of the factor number and the best solution depended upon the following criteria. (1)

196 A lower Q value (Equation 6; a function to evaluate the model runs) was preferable. (2) The ratio

197 between Q $_{robust}$ and Q $_{true}$ was lower than 1.5. In this study, the ratios were 0.8 and 0.9 for the

198 summer and autumn data simulation, respectively. (3) Good agreement was shown between the

199 predicted and observed PM$_{2.5}$. The slope and correlation coefficient (R^2) for the linear regression

200   were 0.91 and 0.86 in summer and 0.95 and 0.98 in autumn, respectively, as shown in Figure S2

201   in the Supplement. The lower R^2 value seen during the summer might be due to the lack of WSI

202   data. (4) The residuals were normally distributed between −3 and 3. Table S2 summarizes the

203   percentage of samples with residuals between −3 and 3 for each species; the lowest percentages

204   were 92.9% and 96.0% for Ni in summer and autumn, respectively. The scaled residuals for

205    $PM_{2.5}$ are shown in Figure S3 in the Supplement. The percentage of residuals between −3 and 3

206   was comparable between summer (97.5%) and autumn (98.1%). Data points not confirming to

207   the residual range (-3 to +3) were removed from the analysis. Finally (5), no correlation was

208   found between the factors, which was achieved by examining the G-space plots and controlled

209   by the FPEAK model runs. Figures S4 and S5 in the Supplement present the G-space plots in

210   summer and autumn, respectively. The low factor contributions and poor correlations indicated

211   that rotational ambiguity was effectively controlled.

212   A bootstrap method was used to estimate the model errors, according to which 95% confidence

213   intervals (CIs) were calculated. The 95% CI for $PM_{2.5}$ was 0.6 μg/m^3 (0.7% of predicted $PM_{2.5}$)

214   in summer and 2.6 μg/m^3 (3.2% of predicted $PM_{2.5}$) in autumn.

215    $$x_{ij} = \sum_{k=1}^{p} g_{ik} f_{kj} + e_{ij} \quad \text{(Eq.5)}$$

216    $$Q = \sum_{i=1}^{n} \sum_{j=1}^{m} \left[\frac{x_{ij} - \sum_{k=1}^{p} g_{ik} f_{kj}}{u_{ij}} \right]^2 \quad \text{(Eq.6)}$$

217   where x_{ij} and u_{ij} are the concentration and uncertainty of j species (total of m) in i sample (total

218   of n), g_{ik} represents the contribution of k_{th} source to i sample, f_{kj} indicates the fraction of j

219   species in k_{th} source, and e_{ij} is the residual for j species in the i sample.

220

221   **3. Results and discussion**

222   **3.1 Concentrations of PM_{10} and $PM_{2.5}$**

223   Table 1 shows the mean concentrations of PM_{10} and $PM_{2.5}$ in Wuhan and other Chinese cities and

224   regions. The mean, maximum and minimum values, and standard deviation or 95% CI were

225   provided if available. In general, the concentrations of airborne particles in Wuhan (135.1 ±4.4

226   and 118.9 ± 3.7 μg/m^3 for PM_{10}; 81.2 ± 2.6 and 85.3 ± 2.6 μg/m^3 for $PM_{2.5}$ in summer and

227   autumn, respectively) were lower than those in northern China (i.e., Beijing and Xi'an),

228   comparable to those in eastern China (i.e., Shanghai and Nanjing), and higher than those in

229   southern China (i.e., Guangzhou and Hong Kong) and Taiwan. Bearing in mind that the sampling

site, period, method, and instrument all interfere with comparisons, the ambient particulate pollution in Wuhan was severe.

From summer to autumn, PM_{10} levels declined considerably from 135.1 ± 4.4 to 118.9 ± 3.7 $\mu g/m^3$, whereas $PM_{2.5}$ remained statistically stable ($p > 0.05$). The higher summer PM_{10} concentration was probably related to a higher load of fugitive dust. In Wuhan, the temperature ($25.6\,°C \pm 0.2\,°C$) in summer was considerably higher than that ($17.5\,°C \pm 0.3\,°C$) in autumn ($p < 0.05$), which led to lower water content in the soil and a higher tendency of dust suspension. In addition, the average wind speed in summer (1.2 ± 0.04 vs. 0.8 ± 0.03 m/s in autumn) was also higher ($p < 0.05$), which could also have favored the generation of fugitive dust.

Table 1. Comparisons of PM_{10} and $PM_{2.5}$ (in $\mu g/m^3$) between Wuhan and other Chinese cities and regions.

	PM_{10}	$PM_{2.5}$	Sampling period
Wuhan	135.1 ± 4.4 [I]	81.2 ± 2.6 [I]	May-Jun. 2014 (this study)
	118.9 ± 3.7 [I]	85.3 ± 2.6 [I]	Oct.-Nov. 2014 (this study)
Beijing	155.9 [II]	73.8 [II]	Jun.-Aug. 2009 [a]
	194.4 [II]	103.9 [II]	Sept.-Nov. 2009 [a]
	133.7 ± 87.8 [III]	71.5 ± 53.6 [III]	2012 whole year [b]
Xi'an	257.8 ± 194.7 [III]	140.9 ± 108.9 [III]	2011 whole year [c]
Shanghai	97.4 to 149.2 [IV]	62.3 to 103.1 [IV]	Jul. 2009-Sept. 2010 [d]
Nanjing	119 to 171 [IV]	87 to 125 [IV]	Jun. 2012 [e]
Guangzhou	23.4 [II]	19.2 [II]	Jun.-Aug. 2010-2013 [f]
	51.0 [II]	41.3 [II]	Sept.-Nov. 2010-2013 [f]
Hong Kong	31.0 ± 16.7 [III]	17.7 ± 12.9 [III]	Jun.-Aug. 2014 [g]
	55.8 ± 23.6 [III]	34.0 ± 17.3 [III]	Sept.-Nov. 2014 [g]
Taiwan	39.5 ± 11.6 [III]	21.8 ± 7.5 [III]	May-Nov. 2011 [h]

[I] mean $\pm 95\%$ confidence interval; [II] arithmetic mean; [III] mean $\pm$ standard deviation; [IV] range.

[a] Liu et al. (2014); [b] Liu et al. (2015); [c] Wang et al. (2015); [d] Wang et al. (2013); [e] Shen et al. (2014); [f] Deng et al. (2015); [g] HKEPD (2014); [h] Gugamsetty et al. (2012).

Figure 2 presents the daily concentrations of PM_{10} and $PM_{2.5}$ during the sampling period in

247   Wuhan, with the National Standard Level II (daily averages of 150 and 75 μg/m^3 for PM$_{10}$ and

248   PM$_{2.5}$, respectively). It was found that the concentrations of PM$_{10}$ and PM$_{2.5}$ frequently exceeded

249   the standard levels, indicating the significance of ambient particulate pollution in Wuhan.

250   Because smaller particles tend to pose more harm to human health and to the atmosphere due to

251   their larger specific surface areas (Yang et al., 2012; Goldberg et al., 2001), and because the

252   chemical compositions in PM$_{10}$ were not analyzed, this study focused mainly on PM$_{2.5}$. During

253   the sampling campaign, six PM$_{2.5}$ episodes, named episodes 1 through 6, with daily averages of

254   PM$_{2.5}$ in excess of 75 μg/m^3, were captured (Figure 2). It should be noted that to ensure the data

255   size of each episode, only the cases in which the daily PM$_{2.5}$ average was consecutively higher

256   than 75 μg/m^3 for 3 days or longer were treated as PM$_{2.5}$ episodes.

257   Table 2 summarizes the concentrations of PM$_{10}$ and PM$_{2.5}$ and the percentage of PM$_{2.5}$ in PM$_{10}$,

258   referred to as PM$_{2.5}$/PM$_{10}$, during the summer and autumn episodes and non-episodes. PM$_{10}$ and

259   PM$_{2.5}$ concentrations increased significantly ($p < 0.05$) during the episodes in both summer and

260   autumn. The PM$_{2.5}$/PM$_{10}$ value also increased remarkably on episode days compared to that on

261   non-episode days, except for episode 2 (45.9% ± 2.5%), which suggests that more secondary

262   species and/or primary fine particles (e.g., primary OC and EC generated from combustion) were

263   generated or released during the episodes. In contrast, the lower PM$_{2.5}$/PM$_{10}$ value during

264   episode 2 might imply a strong source of coarse particles. Indeed, this inference was confirmed

265   by the source apportionment analysis in section 3.3.3.

266
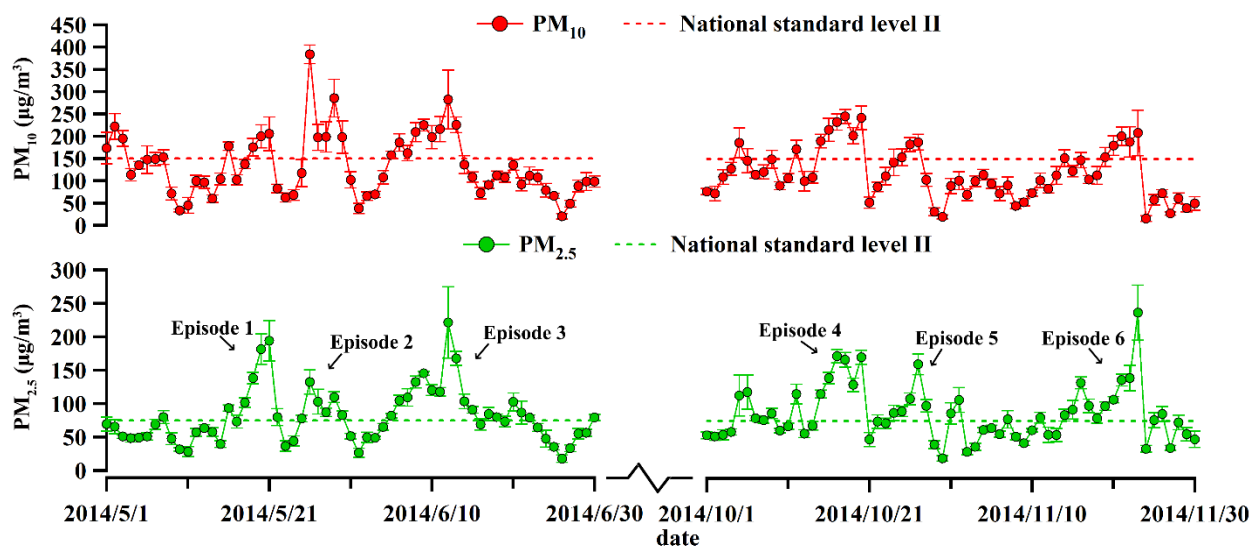
267

268   Figure 2. Daily concentrations of PM$_{10}$ and PM$_{2.5}$ in May, June, October, and November 2014.

269 Episode 1, May 16 to 22; episode 2, May 25 to 30; episode 3, June 5 to 15; episode 4, October

270 15 to 20; episode 5, October 24 to 28; Episode 6, November 14 to 23.

271

272 Table 2. Mean PM_{10}, $PM_{2.5}$, and $PM_{2.5}/PM_{10}$ with 95% CI during $PM_{2.5}$ episodes and non-

273 episodes in Wuhan. Non-episode 1 and Non-episode 2 represent the non-episode periods in

274 summer and autumn, respectively.

	PM_{10} ($\mu g/m^3$)	$PM_{2.5}$ ($\mu g/m^3$)	$PM_{2.5}/PM_{10}$ (%)
Episode 1	154.3 ± 10.1	123.0 ± 9.1	72.8 ± 2.6
Episode 2	230.1 ± 19.1	98.9 ± 5.7	45.9 ± 2.5
Episode 3	191.4 ± 9.8	126.7 ± 7.0	66.9 ± 1.8
Non-episode 1	**98.5 ± 3.9**	**56.6 ± 1.7**	**58.9 ± 1.5**
Episode 4	221.8 ± 8.9	148.6 ± 5.2	67.9 ± 2.0
Episode 5	154.2 ± 10.4	108.2 ± 6.8	69.3 ± 3.1
Episode 6	157.3 ± 9.0	120.0 ± 7.6	71.2 ± 2.1
Non-episode 2	**88.7 ± 3.4**	**64.2 ± 2.2**	**65.3 ± 1.3**

275

276 **3.2 Chemical composition of $PM_{2.5}$**

277 Figure 3 shows the daily variations of $PM_{2.5}$ and its composition. As the instrument for the

278 analysis of WSIs was initially deployed in September 2014, data are not available for May and

279 June. The carbonaceous aerosol (18.5 ± 1.2 $\mu g/m^3$) and elements (6.0 ± 0.3 $\mu g/m^3$) accounted for

280 19.1% ± 0.6% and 6.2% ± 0.2% of $PM_{2.5}$ in summer, respectively. In autumn, WSIs were the

281 most abundant component in $PM_{2.5}$ (64.4 ± 2.5 $\mu g/m^3$; 68.6% ± 1.9%), followed by carbonaceous

282 aerosol (24.3 ± 1.0 $\mu g/m^3$; 25.5% ± 0.8%) and elements (4.5 ± 0.2 $\mu g/m^3$; 4.6% ± 0.1%). The

283 secondary inorganic ions SO_4^{2-} (18.8 ± 0.6 $\mu g/m^3$), NO_3^- (18.7 ± 0.8 $\mu g/m^3$), and NH_4^+ ($12.0 \pm$

284 0.4 $\mu g/m^3$) dominated the WSIs, with the average contribution of 34.0% ± 0.6%, 30.1% ± 0.5%,

285 and 20.4% ± 0.1%, respectively.

286
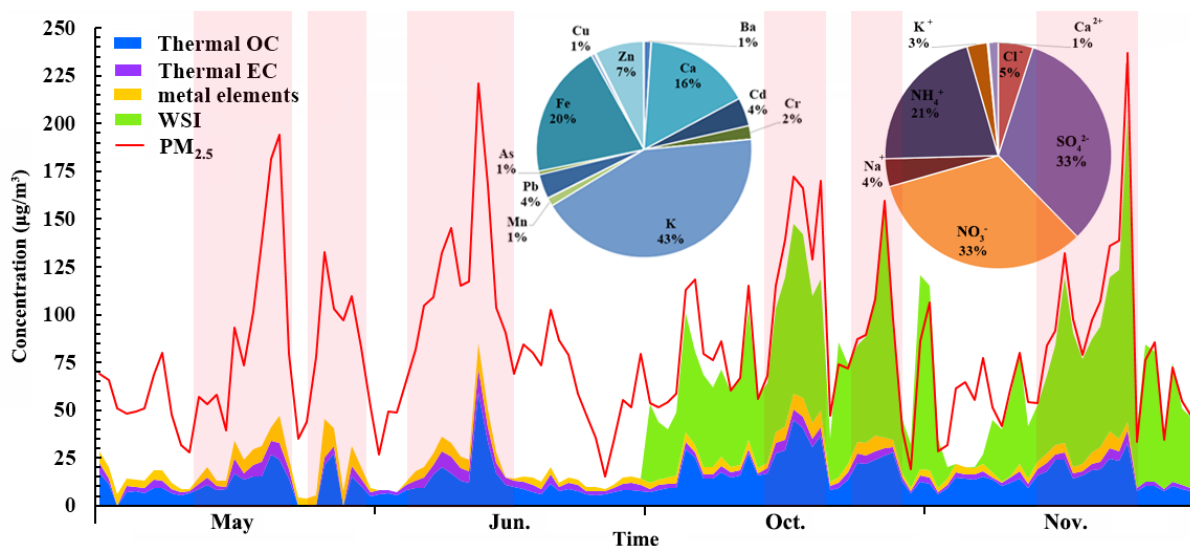
Figure 3. Daily variations of $PM_{2.5}$ and its components. Pie charts represent the composition of elements and water-soluble ions, respectively. Pink shaded areas represent episodes.

The charge balance between the anions and cations was usually used to predict the existing forms of SIAs and the acidity of $PM_{2.5}$. Figure 4 shows the relative abundance of molar charges of SIAs, which were located fairly close to the one-to-one line on both episode and non-episode days. This finding suggests that NH_4NO_3 and $(NH_4)_2SO_4$ were coexisting forms of the SIAs in $PM_{2.5}$ in Wuhan. When extending NH_4^+ to total cations (NH_4^+, Ca^{2+}, Mg^{2+}, Na^+, and K^+) and NO_3^- and SO_4^{2-} to total anions (NO_3^-, SO_4^{2-}, and Cl^-), the molar charges of the cations and anions were balanced (slope, 0.98; $R^2 = 0.98$), as shown in Figure S6 in the Supplement, indicating that $PM_{2.5}$ was neutralized during autumn in Wuhan.
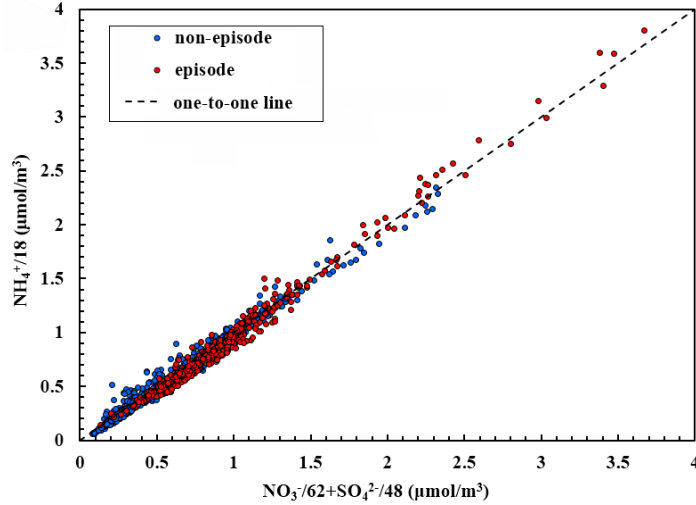
300

301   Figure 4. Relative abundance of molar charges of $PM_{2.5}$ during autumn in Wuhan.

302

303   For the carbonaceous aerosol, OC (14.8 ± 0.5 μg/m³) and EC (3.6 ± 0.1 μg/m³) accounted for

304   79.9% ±0.3% and 20.2% ±0.3% of the total carbon, respectively. In general, SOC was expected

305   to exist when the OC/EC ratio was greater than 2 (Duan et al., 2005; Chow et al., 1996), and the

306   proportion of SOC increased with the increase in OC/EC ratio. The average OC/EC ratio was 4.8

307   ± 0.1 in Wuhan, which suggests that SOC (i.e., carbon fraction of SOA) was an important

308   component in $PM_{2.5}$. Indeed, as the constituents of OC, SOC and POC can be distinguished with

309   the EC-tracer method, following Equations 7 and 8 (Cabada et al., 2004):

310   POC = (OC/EC) $_{prim}$ × EC + OC $_{non\text{-}comb}$ (Eq.7)

311   SOC = OC – POC   (Eq.8)

312   where (OC/EC) $_{prim}$ was the ratio of primary OC to EC, obtained from the pairs of OC and EC

313   with the OC/EC ratios among the 10% lowest; and OC $_{non\text{-}comb}$ was the primary OC that was not

314   related to combustion activities. These values were determined by the slope and intercept of the

315   linear regression between primary OC and EC, respectively (Figure 5). Because the abundance

316   of SOC depended largely upon the oxidative capacity of the atmosphere, the oxidative radical

317   (HO_2) was simulated with the PBM-MCM model and compared with the pattern of SOC. More

318   details about the simulation are provided in section 3.4. Figure 6 shows the hourly concentrations

319   of SOC and POC and the average diurnal patterns of SOC, POC, and HO_2. In general, the POC

320   levels (8.6 ± 0.2 μg/m³) were slightly higher than those of SOC (6.4 ± 0.3 μg/m³; $p < 0.05$). The

321   difference was greatest in November, when the concentration was 9.5 ± 0.4 and 4.7 ± 0.3 μg/m³

322   for POC and SOC, respectively. Because the production of SOC was closely related to the

323 atmospheric oxidative capacity, the lowest fraction of SOC in November might be attributable to
324 the weakest oxidative capacity; for example, the O_3 level was lowest in November (14.3 ± 1.0
325 ppbv). Two peaks were found for the simulated diurnal pattern of HO_2, which might be caused
326 by strong solar radiation at noon and in the early afternoon and by reactions among alkenes and
327 O_3 and NO_3 at night (Emmerson et al., 2005; Kanaya et al., 1999). The diurnal patterns of POC
328 and SOC revealed that POC levels were relatively stable throughout the day. The increase in the
329 POC level in the early morning (06:00 to 08:00) and late afternoon and early evening (16:00 to
330 20:00) was likely related to increases in vehicular emissions during rush hours, and the decrease
331 from 08:00 to 15:00 might be caused by the extension of the boundary layer. In contrast, the
332 SOC level showed two peaks at around 12:00 and 19:00, which was consistent with the diurnal
333 variation of the simulated HO_2, suggesting that the formation of SOC was closely related to the
334 oxidative radicals in the atmosphere. (A detailed relationship is discussed in section 3.4.3.)

335
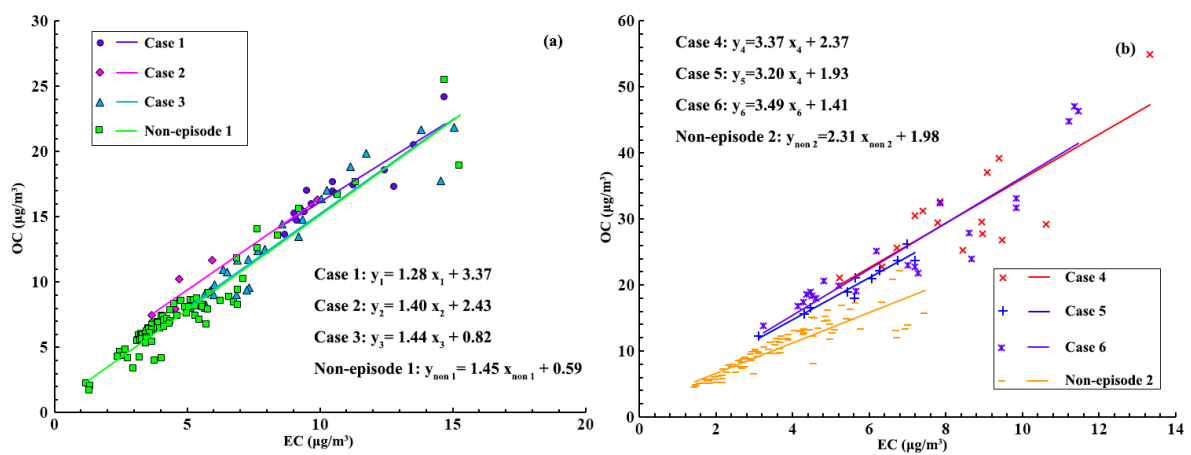
336
337 Figure 5. Regression between OC and EC with the 10% lowest OC/EC ratios during (a) summer
338 and (b) autumn in Wuhan.
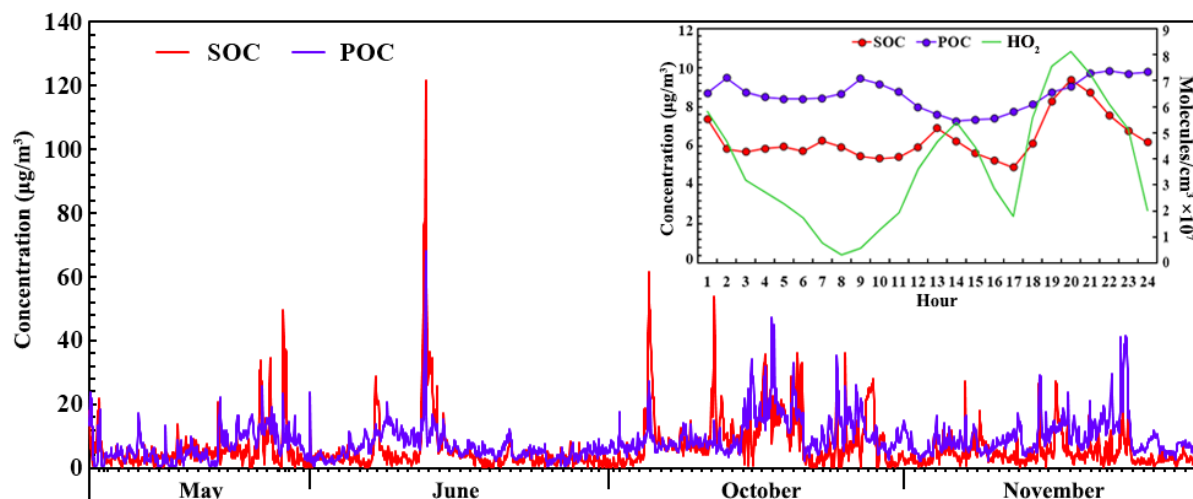
Figure 6. Hourly concentrations of SOC and POC. Insert graph presents average diurnal variations of SOC, POC, and HO$_2$.

Among the elements, potassium (K; 2060.7 $\pm$ 82.3 ng/m^3), iron (Fe; 996.5 $\pm$ 34.3 ng/m^3), and calcium (Ca; 774.1 $\pm$ 39.4 ng/m^3) were the most abundant species, accounting for 47.0% $\pm$ 2.2%, 21.4% $\pm$ 0.3%, and 15.6% $\pm$ 0.3% of the total analyzed elements, respectively. Correlation analysis indicated that Fe had good correlation with Ca (R^2 = 0.66; Figure S7 in the Supplement), whereas weak correlations of K with Fe (R^2 = 0.14) and Ca (R^2 = 0.09) were found, suggesting that Fe and Ca shared common sources that were different from the sources of K. Because Fe and Ca are typical crustal elements, fugitive dust (e.g., dust from traffic, construction and demolition works, yards, and bare soil) was their most likely source. In contrast, apart from emissions from mineral sources, K is also emitted from biomass burning. As such, K was believed to be mainly emitted from biomass burning in this study, which is further supported by the moderate correlations of K with OC (R^2 = 0.52) and EC (R^2 = 0.48) because biomass burning also emits OC and EC (Saarikoski et al., 2007; Echalar et al., 1995).

3.3 Causes of PM$_{2.5}$ episodes

3.3.1 Meteorological conditions

The processes of particle formation, dispersion, and deposition are closely related to meteorological conditions. To interpret the possible causes of the PM$_{2.5}$ episodes, Figure 8 shows the patterns of wind direction and speed, temperature, relative humidity, and atmospheric pressure in Wuhan during the monitoring period. In general, southeast winds prevailed at the sampling site with a wind speed of approximately 1.0 m/s. The low wind speed indicates the

362   dominance of local air masses. However, due to the high stability and long lifetime of $PM_{2.5}$, the

363   regional and superregional impact could not be eliminated. In comparison with those in summer,

364   the wind speed (summer, 1.1 ±0.04 m/s; autumn, 0.8 ±0.03 m/s) and temperature (summer, 25.6

365   ± 0.2 m/s; autumn, 17.5 ±0.3 m/s) were significantly ($p < 0.05$) lower in autumn, whereas the

366   atmospheric pressure (summer, 1006.9 ±0.2 hPa; autumn, 1020.9 ±0.2 hPa) was much higher.

367   During the episodes, the wind speed was generally lower than during non-episodes, with the

368   exception of episode 5. This might be one cause for the episodes, but it does not fully explain the

369   great enhancements of $PM_{2.5}$, because the wind speeds were very low and the differences

370   between the episodes and non-episodes were minor. The atmospheric pressure was not very high

371   during episodes 1 through 5, suggesting that the synoptic system was not responsible for the

372   occurrence of these $PM_{2.5}$ episodes. However, the atmospheric pressure was remarkably higher

373   ($p < 0.05$) in episode 6 (1024 ±1 hPa) than in non-episode 2 (1021 ±0.3 hPa), which might have

374   suppressed the diffusion of $PM_{2.5}$ and the gaseous precursors. In addition, the temperature was

375   lower (episode 6, 14.0 ℃ ±0.4 ℃; non-episode 2, 17.2 ℃ ±0.3 ℃; $p < 0.05$), which favors the

376   gas-to-particle partitioning of semivolatile and non–thermal stabilized species. As a consequence,

377   these effects might have elevated the $PM_{2.5}$ concentrations in episode 6, which is discussed

378   further in section 3.4.2.

379
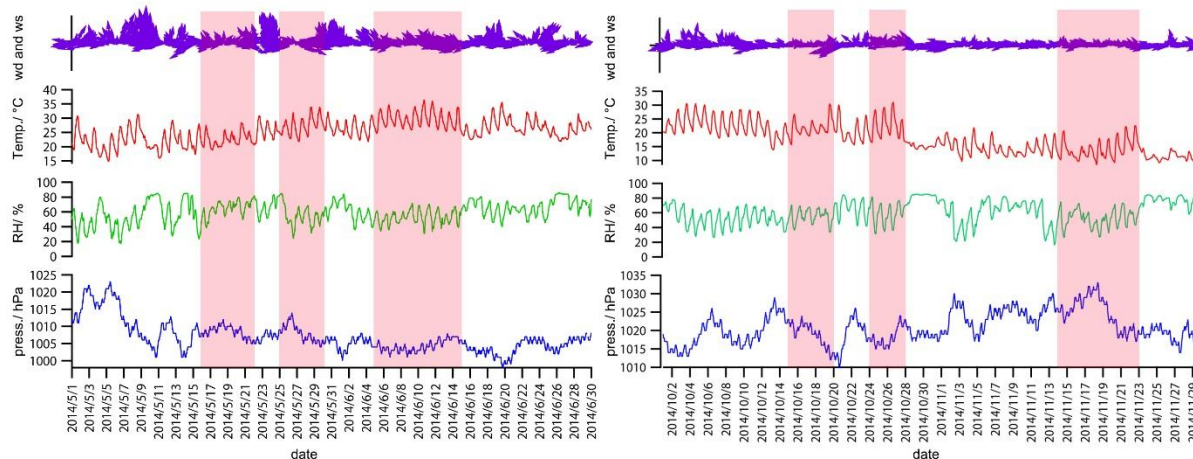
380

381   Figure 8. Meteorological patterns in Wuhan during the monitoring period. Pink shaded areas

382   represent $PM_{2.5}$ episodes.

383

384   **3.3.2 Chemical signatures**

385   Table 3 summarizes the mass concentrations and percentages of the main components in $PM_{2.5}$.

386   The mass concentrations of $PM_{2.5}$ components significantly increased from non-episode days to

387   episode days ($p < 0.05$). In contrast, the percentages of the chemical components in $PM_{2.5}$ varied

388   by species. In summer, the fractions of EC and K in $PM_{2.5}$ experienced significant increases from

389   non-episode 1 (EC, 4.8% $\pm 0.2\%$; K, 2.0% $\pm 0.1\%$) to episode 1 (EC, 5.7% $\pm 0.5\%$; K, 4.4% $\pm$

390   0.3%) and episode 3 (EC, 5.3% $\pm 0.2\%$; K, 3.0% $\pm 0.2\%$). Because EC is the tracer of

391   incomplete combustion (Chow et al., 1996) and K is the indicator of biomass burning (Saarikoski

392   et al., 2007; Echalar et al., 1995), the higher percentages of EC and K in episodes 1 and 3 imply

393   the outstanding contribution of biomass burning. In contrast, the fraction of OC in $PM_{2.5}$

394   remained stable on both episode and non-episode days ($p > 0.05$), possibly because the high

395   temperatures in summer hindered the gas-to-particle partitioning of semivolatile organics

396   (Takekawa et al., 2003). Furthermore, the percentages of Ca (2.9% $\pm 0.4\%$) and Fe (2.7% $\pm 0.3\%$)

397   significantly increased during episode 2 ($p < 0.05$) compared to those in non-episode 1 (Ca, 1.1%

398    $\pm 0.1\%$; Fe, 1.5% $\pm 0.1\%$), which shows that fugitive dust made a considerable contribution to

399    $PM_{2.5}$ in episode 2. In addition, biomass burning might also have contributed to $PM_{2.5}$, in view of

400   the increase in the percentage of K (non-episode 1, 2.0% $\pm 0.1\%$; episode 2, 3.2% $\pm 0.2\%$).

401   In autumn, the percentage of K significantly ($p < 0.05$) increased during episode 4 (3.1% $\pm 0.1\%$

402   vs. 2.1% $\pm 0.1\%$ in non-episode 2), as did that of OC (27.3% $\pm 0.7\%$ vs. 20.9% $\pm 0.8\%$ in non-

403   episode 2), suggesting the dominant role of biomass burning in episode 4. Furthermore, the

404   fractions of OC in episode 5 (23.8% $\pm 1.5\%$) and NO_3^- in episode 6 (26.1% $\pm 1.0\%$) were

405   obviously higher than those in non-episode 2 (OC, 20.9% $\pm 0.8\%$; NO_3^-, 19.8% $\pm 0.9\%$). Due to

406   the complexity of the sources of OC and NO_3^-, the causes of episodes 5 and 6 are further

407   explored in the following sections.

408   In summary, episodes 1, 3, and 4 were greatly affected by biomass burning. This finding was

409   further confirmed by the significant increases in the gaseous tracers of biomass burning such as

410   ethyne (C_2H_2) and methyl chloride (CH_3Cl) (Guo et al., 2011b; Simoneit et al., 2002) during

411   these episodes ($p < 0.05$; see Figure S8 in the Supplement).

412 Table 3. Concentrations (μg/m^3) and percentages (in parentheses) of the main components of PM$_{2.5}$ during non-episodes and episodes.

413 Bold font demonstrates significant increase in percentage of PM$_{2.5}$ components during episodes compared to non-episodes.

	Summer				Autumn			
	Episode 1	Episode 2	Episode 3	Non-episode 1	Episode 4	Episode 5	Episode 6	Non-episode 2
OC	18.5±1.3	16.3±3.3	19.8±2.5	7.9±0.3	**35.1±1.7**	**24.9±1.9**	22.7±1.5	14.6±1.0
	(15.1% ±0.8%)	(14.0% ±1.9%)	(14.5% ±1.0%)	(15.4% ±0.7%)	**(27.3% ±0.7%)**	**(23.8% ±1.5%)**	(21.4% ±0.8%)	(20.9% ±0.8%)
EC	**6.8±0.5**	4.3±0.6	**6.6±0.5**	2.8±0.1	5.4±0.4	4.2±0.4	4.2±0.4	2.7±0.2
	(5.7% ±0.5%)	(4.1% ±0.5%)	**(5.3% ±0.2%)**	(4.8% ±0.2%)	(4.2% ±0.3%)	(4.1% ±0.4%)	(3.9% ±0.2%)	(4.0% ±0.2%)
SO$_4^{2-}$	NA	NA	NA	NA	28.3±0.9	25.9±2.4	21.3±2.0	18.8±0.9
					(22.8% ±0.9%)	(23.7% ±1.1%)	(19.2% ±0.6%)	(26.9% ±0.9%)
NO$_3^-$	NA	NA	NA	NA	23.7±1.9	24.7±2.9	**30.8±3.6**	15.8±1.3
					(17.8% ±0.9%)	(21.4% ±1.1%)	**(26.1% ±1.0%)**	(19.8% ±0.9%)
NH$_4^+$	NA	NA	NA	NA	16.5±0.8	15.6±1.8	16.8±1.8	11.0±0.7
					(12.9% ±0.2%)	(13.7% ±0.6%)	(14.5% ±0.3%)	(14.9% ±0.3%)
K	**5.3±0.6**	**3.4±0.4**	**3.8±0.5**	1.1±0.1	**4.0±0.2**	2.3±0.2	2.4±0.2	1.4±0.1
	(4.4% ±0.3%)	**(3.2% ±0.2%)**	**(3.0% ±0.2%)**	(2.0% ±0.1%)	**(3.1% ±0.1%)**	(2.2% ±0.1%)	(2.2% ±0.1%)	(2.1% ±0.1%)
Ca	1.2±0.4	**3.2±0.4**	0.9±0.3	0.6±0.04	1.1±0.1	0.8±0.2	0.8±0.1	0.3±0.04
	(1.1% ±0.1%)	**(2.9% ±0.4%)**	(0.8% ±0.1%)	(1.1% ±0.1%)	(0.9% ±0.1%)	(0.8% ±0.2%)	(0.8% ±0.1%)	(0.5% ±0.1%)
Fe	1.4±0.1	**2.8±0.3**	1.1±0.1	0.8±0.05	1.5±0.1	1.2±0.2	1.2±0.1	0.6±0.04
	(1.3% ±0.1%)	**(2.7% ±0.3%)**	(1.0% ±0.1%)	(1.5% ±0.1%)	(1.2% ±0.2%)	(1.2% ±0.2%)	(1.1% ±0.1%)	(0.9% ±0.1%)

414

3.3.3 Source apportionment

To clarify the sources of $PM_{2.5}$ and quantify their contributions, the hourly data on $PM_{2.5}$ components were applied to PMF for source apportionment. Five and six sources were resolved for summer and autumn, respectively, as shown in Figure 10 and Figure 11. The source of SIA was missing in summer, due to the lack of WSI data. For other sources, the profile of each corresponding source was similar in summer and autumn. Factor 1 had high loadings of crustal elements (i.e., Ba, Ca, Mn, and Fe), indicating the source of fugitive dust. Factor 2 was likely associated with oil refinery and usage, in view of the high percentages of V and Ni, which often originate from the combustion of heavy oil (Barwise et al., 1990; Nriagu and Pacyna, 1988). Factor 3 was distinguished by the high loadings of OC, EC, and K, indicating the biomass burning source (Zhang et al., 2013; Friedli et al., 2003). Factor 4 seemed to represent vehicle emissions, due to the dominance of Pb, As, Cu, and Se. Cu has been identified as one of the most abundant metals in both brake linings and the brake wear particles with the concentration of up to 210 mg/g in brake wear dust (Grigoratos and Martini, 2015). Although lead-containing gasoline has been forbidden in China since 2000, high levels of Pb are often reported in traffic sources (Yang et al., 2013; Song et al., 2012), which might be due to the use of Pb-containing materials in car components, such as lead wheel weights, solder in electronics, and lead-acid batteries (Song et al., 2012). Both biomass burning and vehicular emissions are important sources of EC. The much lower EC apportioned to vehicular emissions in this study is explained in Section 1 of the Supplement. OC and Hg dominated in factor 5, and Cl^- also showed high loading in this factor in the autumn profile. It is well documented that Hg and Cl^- are largely emitted from coal combustion (Wang et al., 2010; Ye et al., 2003). Hence, this factor was assigned as coal combustion. Finally, a source of SIA with high loadings of NO_3^-, SO_4^{2-}, and NH_4^+ was resolved in autumn.

Figures S9 and S10 in the Supplement show the day-to-day variations of the source contributions in summer and autumn, respectively. Overall, biomass burning was the largest contributor (45.0% $\pm$ 0.03%) to $PM_{2.5}$ in summer. However, the contribution of biomass burning in autumn (23.7% $\pm$ 0.5%) was lower than that of SIA (38.6% $\pm$ 0.7%). Bearing in mind the uncertainties caused by the lack of WSIs, the greater contribution of biomass burning in summer might be associated with the lower WSIs. For example, NO_3^- was expected to be much lower in summer due to its thermal decomposition at high temperatures. Table 4 summarizes the source contributions during

446   episodes and non-episodes. Noticeably, the contributions of biomass burning were significantly

447   higher ($p < 0.05$) in episode 1 (59.2 $\pm$ 6.3 μg/m^3; 46.6% $\pm$ 3.0%), episode 3 (64.9 $\pm$ 3.3 μg/m^3;

448   50.8% $\pm$ 1.2%), and episode 4 (48.7 $\pm$ 2.9 μg/m^3; 44.8% $\pm$ 2.6%) than those in the corresponding

449   non-episodes, confirming that biomass burning was the main cause of these $PM_{2.5}$ episodes. In

450   addition, vehicle emissions made a greater contribution to episode 4 (14.9 $\pm$ 1.2 μg/m^3; 13.7% $\pm$

451   1.1%) than to non-episode 2. In contrast, the contribution of fugitive dust (6.5 $\pm$ 1.3 μg/m^3; 5.6%

452     $\pm$ 1.0%) in episode 2 was remarkably ($p < 0.05$) higher than in non-episode 1 (1.1 $\pm$ 0.1 μg/m^3;

453   1.8% $\pm$ 0.2%). This finding was consistent with the inference that episode 2 was attributable to

454   fugitive dust according to the low $PM_{2.5}/PM_{10}$ ratio (45.9% $\pm$ 2.5%) and high levels of crustal

455   elements (Ca, 2.9% $\pm$ 0.4%; Fe, 2.7% $\pm$ 0.3%) in this episode. In addition, vehicle emissions and

456   SIA both experienced significant increases in episodes 5 and 6 ($p < 0.05$). In fact, the increase of

457   OC in episode 5 (see Table 3) was mainly caused by vehicle emissions and coal combustion

458   (Table S3 in the Supplement). For episode 6, in addition to the increase in OC, SIA was also an

459   important contributor, particularly for NO_3^-, which increased from 9.9 $\pm$ 1.2 μg/m^3 in non-

460   episode 2 to 21.4 $\pm$ 3.3 μg/m^3 in episode 6 (Table S3). In addition, we noted that the contribution

461   of coal combustion was much lower in non-episode 2 than that in non-episode1 ($p<0.05$). The

462   explanation is provided in Section 2 of the Supplement.
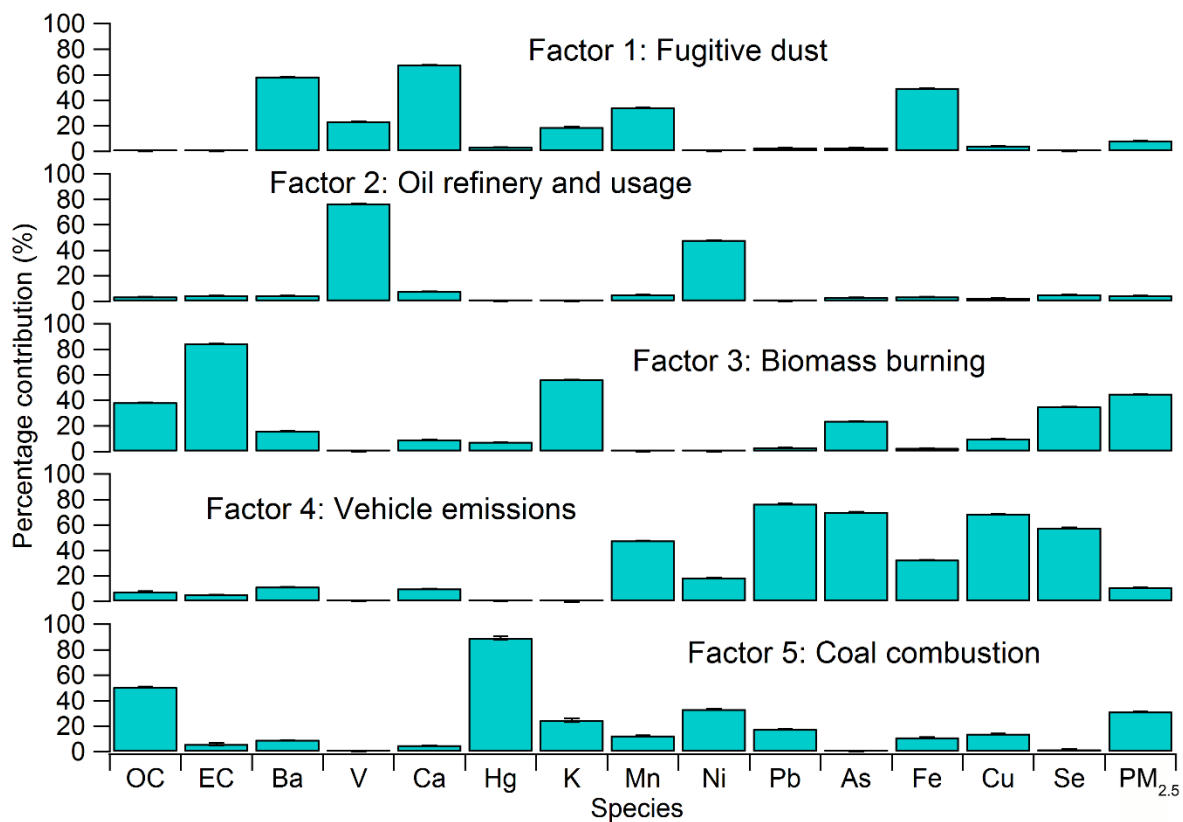
463

464 Figure 10. Profiles of PM$_{2.5}$ sources in summer. Error bars represent 95% CI estimated by

465 bootstrap method in PMF.
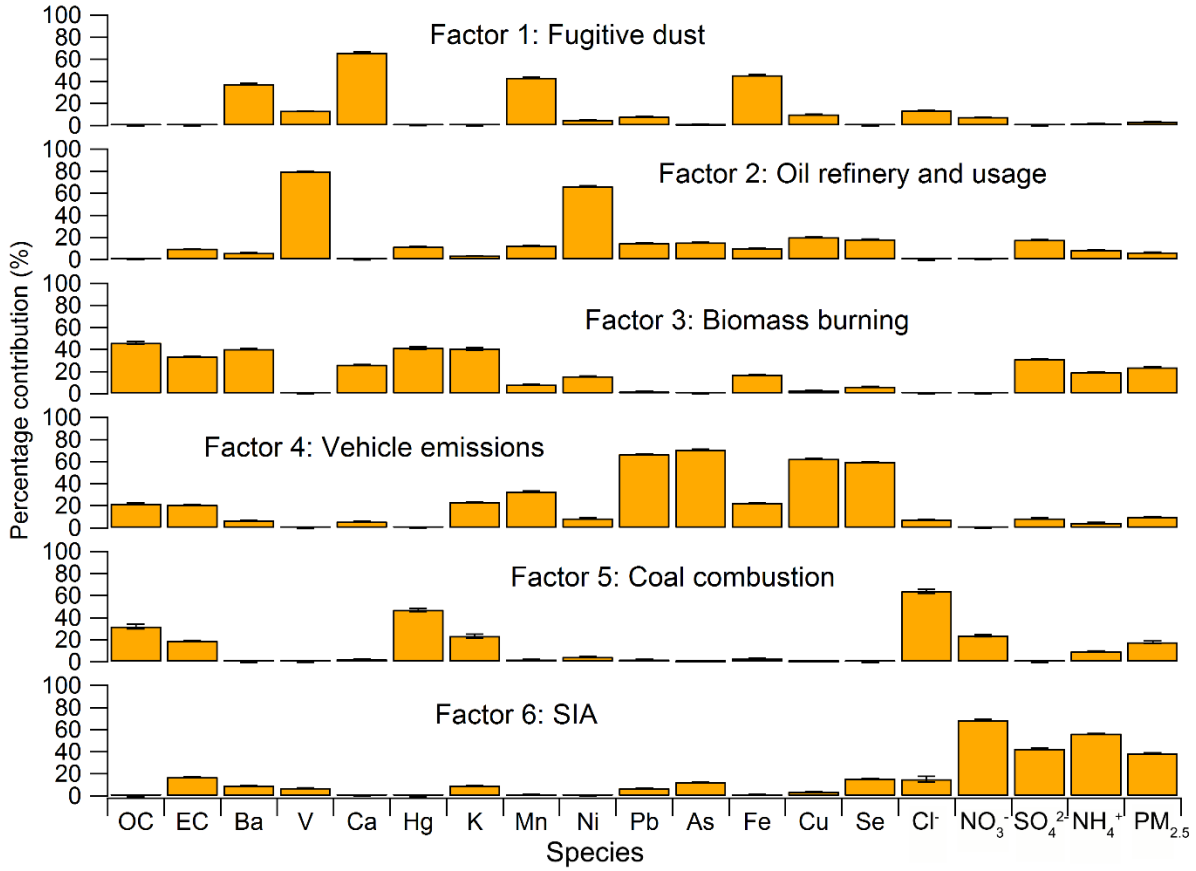
466

467 Figure 11. Profiles of PM$_{2.5}$ sources in autumn. Error bars represent 95% CI estimated by

468 bootstrap method in PMF.

469 Table 4. Mass concentration ($\mu g/m^3$) and percentage contribution (in parentheses) of sources to sum of resolved species in $PM_{2.5}$. Bold

470 font represents a significant increase in percentage contribution in episodes compared to non-episodes.

	Fugitive dust	Oil refinery and usage	Biomass burning	Vehicle emissions	Coal Combustion	SIA
Episode 1	10.0±1.3	4.0±1.2	**59.2±6.3**	12.2±1.8	36.0±2.7	—
	(8.7% ±1.2%)	(2.8% ±0.7%)	**(46.6% ±3.0%)**	(9.6% ±1.2%)	(32.2% ±2.5%)	
Episode 2	**29.5±6.1**	8.2±2.6	37.1±5.8	10.8±3.1	20.9±4.7	—
	(27.5% ±5.5%)	(6.7% ±1.7%)	(35.3% ±4.8%)	(11.9% ±3.2%)	(18.7% ±3.1%)	
Episode 3	6.4±0.5	4.9±1.0	**64.9±3.3**	8.8±0.9	41.6±3.3	—
	(5.3% ±0.4%)	(3.9% ±0.7%)	**(50.8% ±1.2%)**	(7.9% ±0.9%)	(32.1% ±1.5%)	
Non-episode 1	4.8±0.6	2.9±0.4	22.2±1.6	9.3±0.6	19.5±1.0	—
	(8.7% ±1.0%)	(5.0% ±0.7%)	(35.2% ±1.9%)	(16.3% ±1.0%)	(35.9% ±1.7%)	
Episode 4	3.3±0.3	7.2±0.6	**48.7±2.9**	**14.9±1.2**	13.8±1.7	23.3±3.3
	(3.0% ±0.2%)	(7.0% ±0.8%)	**(44.8% ±2.6%)**	**(13.7% ±1.1%)**	(11.9% ±1.3%)	(19.6% ±2.6%)
Episode 5	2.3±0.5	5.3±0.6	21.1±2.8	**12.2±1.9**	14.8±2.0	**39.9±6.4**
	(2.7% ±0.5%)	(6.6% ±0.8%)	(22.1% ±2.3%)	**(13.85±2.1%)**	(17.5% ±2.7%)	**(37.2% ±3.0%)**
Episode 6	2.6±0.3	4.7±0.6	18.4±2.4	**14.2±1.3**	17.7±2.5	**44.6±6.8**
	(3.0% ±0.3%)	(4.7% ±0.4%)	(21.2% ±2.5%)	**(16.1% ±1.3%)**	(16.3% ±1.7%)	**(38.7% ±2.2%)**
Non-episode 2	0.9±0.1	4.7±0.3	22.2±1.6	4.2±0.4	9.8±0.8	20.5±2.5
	(1.6% ±0.2%)	(8.6% ±0.6%)	(39.3% ±2.5%)	(7.4% ±0.7%)	(18.1% ±1.8%)	(25.0% ±2.3%)

471

3.3.4 Open fires and air mass trajectories

To further confirm the biomass burning activities during the PM$_{2.5}$ episodes, the wildfire distribution (downloaded from NASA Firms Web Fire Mapper, and accessible at https://firms.modaps.eosdis.nasa.gov/firemap/) and 72-h backward air mass trajectories (simulated by Hysplit v4.9 model) are plotted in Figure 12. Because the concentrations, compositions and source contributions of PM$_{2.5}$ were averaged over the entire period of each episode, the wildfire distribution and backward trajectories were also averaged for the entire period of each episode. Consistent with the great contributions to PM$_{2.5}$ of biomass burning, the air masses arriving in Wuhan had passed over the areas where intensive open fires were detected in episodes 1, 3, and 4. In episode 2, wildfires were widespread in northeast China. However, the air mass trajectories were mainly from the south and northwest and evaded the burning areas, which might explain why biomass burning was not a predominant factor in episode 2. The sparse wildfires in episodes 5 and 6 coincided with the source apportionment result that biomass burning did not significantly elevate the concentration of PM$_{2.5}$.

Figure 12. Wildfire distribution and 72-h backward air mass trajectories. Red squares demonstrate potential areas where biomass burning aggravated particulate pollution in Wuhan.

491 **3.4 Formation mechanisms**

492 **3.4.1 Model validation**

493 In this study, the PBM-MCM model was used to help investigate the formation mechanisms of

494 NO_3^- and SOC. Before application, the model was validated via O_3 simulation. Figure S11

495 compares the daily averages and diurnal variations of O_3 between the simulation and the

496 observations. It was found that the model simulated O_3 variation well in both daily and diurnal

497 patterns. However, it generally overestimated the O_3 levels in November. The meteorological

498 parameters indicated that the frequency of foggy days was extremely high (36.7%) in November,

499 possibly resulting in a weakening of solar radiation and consequently of photochemical reactivity.

500 To quantitatively evaluate the performance of the model, the index of agreement (IOA) was

501 calculated using Equation 9.

502
$$IOA = 1 - \frac{\sum_{i=1}^{n}(O_i - S_i)^2}{\sum_{i=1}^{n}(|O_i - \bar{O}| + |S_i - \bar{O}|)^2} \quad (Eq.9)$$

503 where $\bar{O}$ is the average of n samples and O_i and S_i represent the observed and simulated values,

504 respectively. Within the interval of [0, 1], higher IOA values indicated better agreement between

505 the simulation and observation.

506 By calculation, the IOA reached 0.86, indicating excellent performance of the model in the O_3

507 simulation. Because O_3 production is closely associated with oxidative radicals, intermediates,

508 and products, the robust O_3 simulation gave us full confidence to accept the simulated N_2O_5,

509 HO_2, and SVOCs.

510

511 **3.4.2 NO_3^- formation**

512 The composition analysis indicated that the proportion of NO_3^- increased remarkably during

513 episode 6. To interpret this phenomenon, the formation mechanisms of NO_3^- were investigated.

514 Figure 14 shows the hourly variations of the calculated and observed NO_3^- and the contribution

515 of R3 (i.e., $N_2O_5 + H_2O \rightarrow 2HNO_3$), among which $NO_3^-_{cal\ 1}$, $NO_3^-_{cal\ 2}$, and $NO_3^-_{obs}$ referred to

516 homogeneous formation (R1 and R2), total formation (R1, R2, and R3), and field measurement

517 of NO_3^-, respectively. Although the particle-bound NO_3^- was influenced by many factors (i.e.,

518 formation, deposition, and dispersion), the calculations generally well reproduced the measured

519 NO_3^- in episode 6, with a high correlation coefficient ($R^2 = 0.63$) and an IOA of 0.78. However,

520 on November 23, 2014, the observed NO_3^- decreased rapidly from 09:00, which was not

521 captured by the calculations. This discrepancy was likely caused by the weather conditions on

522   that day, because (1) the average wind speed increased from 1.7 m/s before 09:00 to 2.7 m/s after
523   09:00 and even reached 4.0 m/s at 14:00; and (2) moderate rain began at 12:00 and continued
524   until 23:00, with total precipitation of 24 mm. Indeed, this was the beginning of a 7-day rainy
525   period, which ended episode 6 with a sharp decrease of the $PM_{2.5}$ concentration (approximately
526   175 μg/m^3; see Figure 2).

527   Because the values of $NO_3^-{}_{cal\ 1}$ were very close to those of $NO_3^-{}_{cal\ 2}$, the variation of NO_3^- in
528   episode 6 could be well explained by the homogeneous formation (R1 and R2), whereas the
529   heterogeneous reaction of N_2O_5 on aerosol surfaces (R3) made only a minor contribution to the
530   total NO_3^- (i.e., nearly nil from 0:00 to 17:00 and 3.7% ± 0.6% from 18:00 to 23:00). Because
531   the homogeneous formation of NO_3^- was closely related to the concentrations of HNO_3 (g) and
532   NH_3 (g) and the temperature (see R1 and R2), Table 4 compares the temperature, HNO_3 (g), NH_3
533   (g), NO, NO_2, O_3, and the simulated OH and HO_2 (a measure of oxidative capacity [Cheng et al.,
534   2010]) between episode 6 and non-episode 2. It was found that the levels of HNO_3 (g) (0.65 ±
535   0.01 ppbv) and NH_3 (g) (13.48 ± 0.72 ppbv) in episode 6 were significantly higher than those
536   during the non-episode 2 (0.47 ± 0.03 and 9.54 ± 0.37 ppbv for HNO_3 and NH_3, respectively),
537   which might substantially favor the formation of NH_4NO_3. Because HNO_3 (g) is generally
538   formed by oxidation of NO_x, the production of HNO_3 (g) should be closely related to the
539   oxidative capacity of the air and the level of NO_x. In episode 6, the levels of O_3 (17.09 ± 2.04
540   ppbv), OH ([3.8 ± 1.3] × 10^5 molecules/cm^3), and HO_2 ([1.1 ± 0.3] × 10^7 molecules/cm^3) were
541   noticeably lower than those in non-episode 2 (O_3, 24.57 ± 1.64 ppbv; OH, [7.2 ± 0.9] × 10^5
542   molecules/cm^3; HO_2, [2.0 ± 0.2] × 10^7 molecules/cm^3), indicating a weaker oxidative capacity.
543   However, the levels of NO (43.55 ± 11.65 ppbv) and NO_2 (44.93 ± 2.29 ppbv) were much higher
544   than those in non-episode 2 (14.70 ± 2.40 and 29.46 ± 0.95 ppbv for NO and NO_2, respectively),
545   possibly leading to the enhancement of HNO_3 (g) in episode 6. Furthermore, the particle-bound
546   NO_3^- was of low thermal stability (Querol et al., 2004), and the temperature lowered ~2.3 C° in
547   episode 6, which suppressed the decomposition and volatilization of NH_4NO_3. Therefore, the
548   high levels of NO_x and NH_3 and the low temperature were both responsible for the increase in
549   NO_3^- in episode 6.
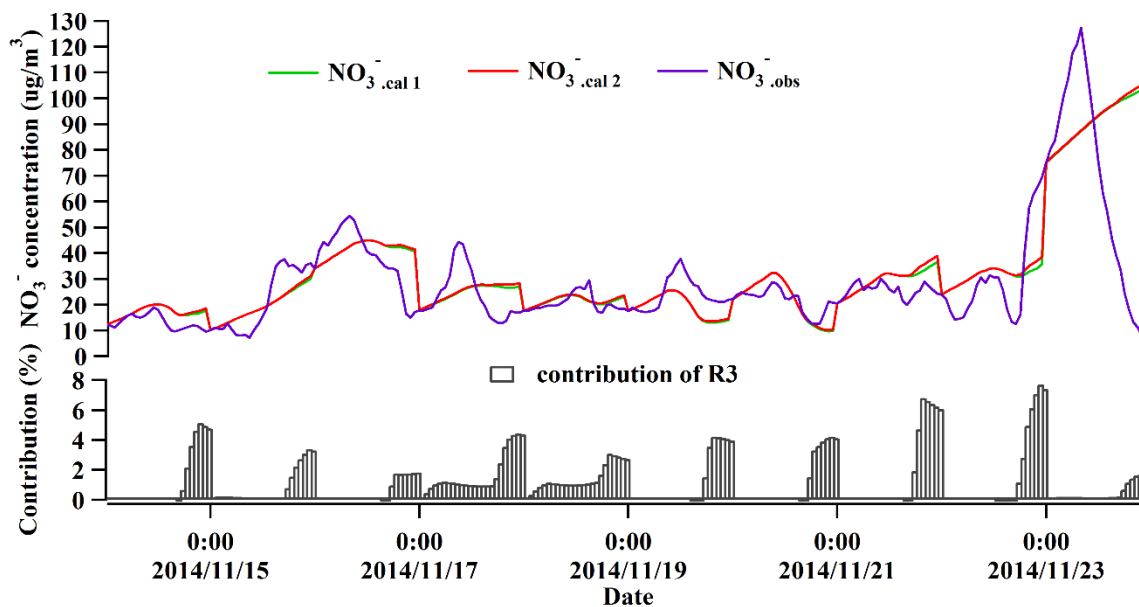
Figure 14. Comparison of NO_3^- between theoretical calculations and observation in episode 6.

Table 4. Comparison of temperature, HNO_3 (g), NH_3 (g), NO, NO_2, O_3, and simulated OH and HO_2 between episode 6 and non-episode 2.

	Episode 6	Non-episode 2
Temperature (°C)	14.9 ± 0.5	17.2 ± 0.3
HNO_3 (ppbv)	0.65 ± 0.01	0.47 ± 0.03
NH_3 (ppbv)	13.48 ± 0.72	9.54 ± 0.37
NO (ppbv)	43.55 ± 11.65	14.70 ± 2.40
NO_2 (ppbv)	44.93 ± 2.29	29.46 ± 0.95
O_3 (ppbv)	17.09 ± 2.04	24.57 ± 1.64
OH (molecules/cm^3)	$(3.8 \pm 1.3) \times 10^5$	$(7.2 \pm 0.9) \times 10^5$
HO_2 (molecules/cm^3)	$(1.1 \pm 0.3) \times 10^7$	$(2.0 \pm 0.2) \times 10^7$

3.4.3 SOC formation

In addition to the high levels of NO_3^- in episode 6, the proportions of OC also increased during the autumn episodes. Because SOC is an important fraction in OC that often grows as an air mass ages, it could help to explain the increase of OC in the autumn episodes by exploring the possible formation mechanisms of SOC. It is well known that SOC formation is closely related

561   to SVOCs, which are formed from the reactions with oxidative radicals (i.e., RO_2, NO_3, and HO_2;

562   Kanakidou et al., 2005; Forstner et al., 1997). Hence, the relationship between SOC and SVOCs

563   was investigated. The SVOCs were simulated with the PBM-MCM model and SOC was

564   calculated with the EC-tracer method mentioned in section 3.2.1. The speciation of SVOCs and

565   their precursors can be found in the Table S4 in the Supplementary Material. Briefly, the

566   precursors of SVOCs include isoprene, aromatics, and C_7-C_{12} n-alkanes.

567   Figure 15 presents the daily and diurnal variations in SOC and SVOCs. It was found that SOCs

568   correlated well with SVOCs in both daily ($R^2 = 0.52$) and diurnal ($R^2 = 0.63$) patterns in autumn,

569   indicating that the simulated SVOCs were responsible for the production of SOC. The oxidation

570   products of aromatics and isoprene were the main constituents of the SVOCs, with average

571   contributions of 42.5% $\pm 2.8\%$ and 39.4% $\pm 2.0\%$, respectively. Among the aromatics, xylenes

572   made the greatest contribution (15.0% $\pm 0.7\%$) to the SVOCs, followed by trimethylbenzenes

573   (11.5% $\pm 0.7\%$), ethylbenzene (8.8% $\pm 0.5\%$), toluene (5.1% $\pm 0.7\%$), and benzene (2.2% $\pm$

574   0.2%). Compared to those in non-episode 2 (i.e., 40.7% $\pm 3.4\%$ and 41.1% $\pm 2.4\%$ contributed

575   by aromatics and isoprene, respectively), the contribution of aromatics to SVOCs increased to

576   46.3% $\pm 4.1\%$ during the episodes, whereas the proportion of isoprene oxidation products

577   decreased to 36.1% $\pm 3.7\%$, suggesting that the increase in aromatics was the main cause of the

578   autumn episodes. To quantify the contribution of biomass burning to SOC, the observed VOCs

579   were apportioned to different sources, including biomass burning with CH_3CN as the tracer. The

580   source profiles are provided in Figure S12 in the Supplementary Material. According to the

581   SVOCs simulated on the basis of VOCs emitted from biomass burning, the SVOCs were

582   elevated by 15.4% $\pm 1.3\%$ due to biomass burning during the episodes.

583   In contrast, the correlations were much worse in summer ($R^2 = 0.01$ and 0.31 for daily and

584   diurnal variations, respectively). The high frequency (50.8%) of rainy days in summer was a

585   factor for the poor correlation; for example, the level of SOC was low during the late period of

586   June when the precipitation lasted for about 10 days, and the model overestimated the SVOCs

587   without considering the influence of precipitation. The correlations between SOC and SVOCs

588   ($R^2 = 0.14$ and 0.19 for the daily and diurnal variations, respectively) were still poor even after

589   the rainy days were excluded. Hence, the poor correlation should also be related to other factors,

590   such as incomplete consideration of the contribution of biogenic VOCs. Although isoprene was

591   included as a precursor of the SVOCs, other biogenic species (i.e., α-pinene, β-pinene, and

592 monoterpenes) that were proven to be important precursors of SOC (Kanakidou et al., 2005)

593 were not monitored in this study. Moreover, the level of biogenic VOCs was much higher in

594 summer than in autumn. Taking isoprene as an example, the mixing ratio of isoprene was 66.7 $\pm$

595 4.9 pptv in summer and only 37.2 $\pm$ 2.6 pptv in autumn. The higher missing level of biogenic

596 VOCs in summer led to a higher deficit of SVOCs, perhaps causing the poorer correlation

597 between SOC and SVOCs. Nevertheless, this notion needs requires validation with more

598 comprehensive data on biogenic VOCs.

599
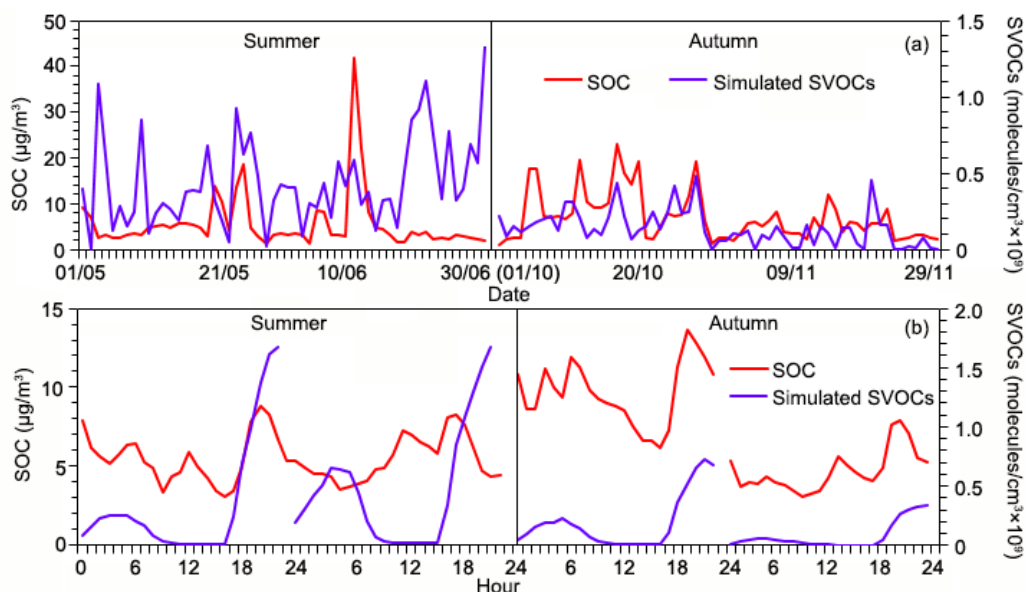
600

601 Figure 14. Correlations between calculated SOC and simulated SVOCs in (a) day-to-day

602 variation and (b) diurnal pattern.

603

604 **4. Conclusions**

605 In summer and autumn 2014, the concentrations of $PM_{2.5}$ and its components were continuously

606 monitored in Wuhan; six $PM_{2.5}$ episodes were captured. The analysis of $PM_{2.5}$ concentrations and

607 compositions found that Wuhan suffered from relatively high levels of $PM_{2.5}$, even in the warm

608 seasons. Secondary inorganic ions were the most predominant species in $PM_{2.5}$ in the form of

609 NH_4NO_3 and $(NH_4)_2SO_4$. Comparable levels of SO_4^{2-} and NO_3^- indicate that stationary and

610 mobile sources had equivalent importance in Wuhan. With the EC-tracer method, it was found

611 that the POC level was slightly higher than that of SOC, and both increased significantly during

612 the episodes. K was the most abundant element in $PM_{2.5}$, implying biomass burning in and

613 around Wuhan during the sampling campaign. Indeed, the source apportionment revealed that
614 biomass burning was the main cause of increases in $PM_{2.5}$ in episodes 1, 3, and 4. Fugitive dust
615 was the leading factor in episode 2. However, episodes 5 and 6 were mainly attributable to
616 vehicle emissions and SIAs. Study of the formation mechanism of NO_3^- and SOC found that
617 NO_3^- was mainly generated from the homogeneous reactions in episode 6, and the high levels of
618 NO_x and NH_3 and the low temperature caused the increase in NO_3^-. Furthermore, the daily and
619 diurnal variations of SOC correlated well with those of SVOCs in autumn. Aromatics and
620 isoprene were the main precursors of SOC, and the contribution of aromatics increased during
621 the episodes. However, the correlation between SOC and SVOCs was much worse in summer,
622 possibly as a result of the incompleteness of the biogenic VOC input in the simulation of SVOCs.
623 This study advances our understanding of the chemical characteristics of $PM_{2.5}$ in warm seasons
624 in Wuhan and for the first time quantifies the contribution of biomass burning to $PM_{2.5}$. The
625 investigation of SOC formation will also inspire the application of the explicit chemical
626 mechanisms on the study of SOA.

627

628 **Acknowledgments:** This study was supported by the Research Grants Council of the Hong
629 Kong Special Administrative Region via grants PolyU5154/13E, PolyU152052/14E,
630 CRF/C5022-14G, and CRF/C5504-15E and the Hong Kong Polytechnic University PhD
631 scholarships (project #RTUP). This study is partly supported by the Hong Kong PolyU internal
632 grant (1-ZVCX and 4-BCAV) and the National Natural Science Foundation of China (No.
633 41275122).

634

635 **References**

636 Anderson, J.O., Thundiyil, J.G., and Stolbach, A., 2012: Clearing the air: A review of the effects
637   of particulate matter air pollution on human health. J. Med. Toxicol. 8, 166-175.
638 Aumont, B., Madronich, S., Ammann, M., Kalberer, M., Baltnesperger, U., Hauglustaine, D., and
639   Baltensperger, F., 1999: On the NO_2 + soot reaction in the atmosphere. J. Geophys. Res. 104,
640   1729-1736.
641 Barwise, A.J.G., 1990: Role of nickel and vanadium in petroleum classification. Energy & Fuels
642   4, 647-652.
643 Brown, S.G., Frankel, A., and Hafner, H.R., 2007: Source apportionment of VOCs in Los

644   Angeles area using positive matrix factorization. Atmos. Environ. 41, 227-237.

645 Cabada, J.C., Pandis, S.N., Subramanian, R., Robinson, A.L., Polidori, A., and Turpin, B., 2004:

646   Estimating the secondary organic aerosol contribution to $PM_{2.5}$ using the EC tracer method.

647   Aerosol Sci. Tech. 38, 140-155.

648 Cao, J.J., Shen, Z.X., Chow, J.C., Watson, J.G., Lee, S.C., Tie, X.X., Ho, K.F., Wang, G.H., and

649   Han, Y.M., 2012: Winter and summer $PM_{2.5}$ chemical compositions in fourteen Chinese cities.

650   J. Air Waste Manage. Assoc. 62, 1214-1226.

651 Cao, J.J., Wu, F., Chow, J.C., Lee, S.C, Li, Y., Chen, S.W., An, Z.S., Fung, K.K., Watson, J.G.,

652   Zhu, C.S., and Liu, S.X., 2005: Characterization and source apportionment of atmospheric

653   organic and elemental carbon during fall and winter of 2003 in Xi'an, China. Atmos. Chem.

654   Phys. 5, 3127-3137.

655 Cheng, H.R., Gong, W., Wang, Z.W., Zhang, F., Wang, X.M., Lv, X.P., Liu, J., Fu, X.X., and

656   Zhang, G., 2014: Ionic composition of submicron particles ($PM_{1.0}$) during the long-lasting

657   haze period in January 2013 in Wuhan, central China. J. Environ. Sci. 26(4), 810-817.

658 Cheng, H.R., Guo, H., Wang, X.M., Saunders, S.M., Lam, S.H.M., Jiang, F., Wang, T.J., Ding,

659   A.J., Lee, S.C., and Ho, K.F., 2010: On the relationship between ozone and its precursors in

660   the Pearl River Delta: application of an observation-based model (OBM). Environ. Sci. Pollut.

661   Res. 17, 547-560.

662 Chow, J.C, Watson, J.G., Lu, Z.Q., Lowenthal, D.H., Frazier, C.A., Solomon, P.A., Thuillier,

663   R.H., and Magliano, K., 1996: Descriptive analysis of $PM_{2.5}$ and PM_{10} at regionally

664   representative locations during SJVAQS/AUSPEX. Atmos. Environ. 30(12), 2079-2112.

665 Deng, X.J., Li, F., Li, Y.H., Li, J.Y., Huang, H.Z., and Liu, X.T., 2015: Vertical distribution

666   characteristics of PM in the surface layer of Guangzhou. Particuology 20, 3-9.

667 Deng, X.J., Tie, X.X., Zhou, X.J., Wu, D., Zhong, L.J., Tan, H.B., Li, F., Huang, X.Y., Bi, X.Y.,

668   and Deng, T., 2008: Effects of Southeast Asia biomass burning on aerosols and ozone

669   concentrations over the Pearl River Delta (PRD) region. Atmos. Environ. 43(36), 8493-8501.

670 Duan, F.K., He, K.B., Ma, Y.L., Jia, Y.T., Yang, F.M., Lei, Y., Tanaka, S., and Okuta, T., 2005:

671   Characteristics of carbonaceous aerosols in Beijing, China. Chemosphere 60(3), 355-364.

672 Echalar, F., Gaudichet, A., Cachier, H., and Artaxo, P., 1995: Aerosol emissions by tropical forest

673   and savanna biomass burning: characteristic trace elements and fluxes. Geophys. Res. Lett. 22,

674   3039-3042.

675   Emmerson, K.M., Carslaw, N., Carpenter, L.J., Heard, D.E., Lee, J.D., and Pilling, M.J., 2005.

676   Urban atmospheric chemistry during the PUMA campaign 1: Comparison of modelled OH and

677   HO_2 concentrations with measurements. J. Atmos. Chem. 52, 143-164.

678   Forstner, H.J.L., Flagan, R.C., and Seinfeld, J.H., 1997: Secondary organic aerosol from the

679   photooxidation of aromatic hydrocarbons: molecular composition. Environ. Sci. Technol. 31

680   (5), 1345-1358.

681   Friedli, H.R., Radke, L.F., Lu, J.Y., Banic, C.M., Leaitch, W.R., and MacPherson, J.I., 2003:

682   Mercury emissions from burning of biomass from temperate North American forests:

683   laboratory and airborne measurements. Atmos. Environ. 37, 253-267.

684   GB 3095-2012, accessible from http://kjs.mep.gov.cn/ hjbhbz/ bzwb/ dqhjbh/ dqhjzlbz/ 201203/

685   W020120410330232398521.pdf.

686   Geng, F.H., Zhang, Q., Tie, X.X., Huang, M.Y., Ma, X.C., Deng, Z.Z., Yu, Q., Quan, J.N., and

687   Zhao, C.S., 2009: Aircraft measurements of O_3, NO_x, CO, VOCs, and SO_2 in the Yangtze

688   River Delta region. Atmos. Environ. 43, 584-593.

689   Goldberg, M.S., Burnett, R.T., Bailar III, J.C., Brook, J., Bonvalot, Y., Tamblyn, R., Singh, R.,

690   and Valois, M.F., 2001: The association between daily mortality and ambient air particle

691   pollution in Montreal, Quebec: 1. Nonaccidental mortality. Environ. Res. 86(1), 12-25.

692   Grigoratos, T., and Martini, G., 2015. Brake wear particle emissions: a review. Environ. Sci.

693   Pollut. Res. 22, 2491-2504.

694   Gugamsetty, B., Wei, H., Liu, C.N., Awasthi, A., Hsu, S.C., Tsai, C.J, Roan, G.D., Wu, Y.C., and

695   Chen, C.F., 2012: Source Characterization and Apportionment of PM_{10}, $PM_{2.5}$ and $PM_{0.1}$ by

696   Using Positive Matrix Factorization. Aerosol Air Qual. Res. 12, 476-491.

697   Guo, H., Cheng, H.R., Ling, Z.H., Louie, P.K.K., and Ayoko, G.A., 2011b: Which emission

698   sources are responsible for the volatile organic compounds in the atmosphere of Pearl River

699   Delta? J. Hazard. Mater. 188, 116-124.

700   Guo, H., Zou, S.C., Tsai, W.Y., Chan, L.Y., and Blake, D.R., 2011a: Emission characteristics of

701   nonmethane hydrocarbons from private cars and taxis at different driving speeds in Hong

702   Kong. Atmos. Environ. 45, 2711-2721.

703   Ho, K.F., Lee, S.C., Chan, C.K., Yu, J.C., Chow, J.C., and Yao, X.H., 2003: Characterization of

704   chemical species in $PM_{2.5}$ and PM_{10} aerosols in Hong Kong. Atmos. Environ. 37(1), 31-39.

705   HKEPD,   2014.   Air   Quality   in   Hong   Kong   2014,   accessible   at

http://www.aqhi.gov.hk/en/download/air- quality-reportse469.html?showall=&start=1.

Hu, J.H., and Abbatt, J.P.D., 1997: Reaction probabilities for N_2O_5 hydrolysis on sulfur acid and ammonium sulfate aerosols at room temperature. J. Phys. Chem. 101A, 871-878.

Kanakidou, M., Seinfeld, J.H., Pandis, S.N., Barnes, I., Dentener, F.J., Facchini, M.C., Dingenen, R.V., Ervens, B., Nenes, A., Nielsen, C.J., Swietlicki, E., Putaud, J.P., Balkanski, Y., Fuzzi, S., Horth, J., Moortgat, G.K., Winterhalter, R., Myhre, C.E.L., Tsigaridis, K., Vignati, E., Stephanou, E.G., and Wilson, J., 2005: Organic aerosol and global climate modelling: a review. Atmos. Chem. Phys. 5, 1053-1123.

Kanaya, Y., Sadanaga, Y., Matsumoto, J., Sharma, U.K., Hirokawa, J., Kajii, Y., and Akimoto, H., 1999: Nighttime observation of the HO_2 radical by an LIF instrument at Oki Island, Japan, and its possible origins. Geophys. Res. Lett. 26, 2179-2182.

Kang, H.Q., Zhu, B., Su, J.F., Wang, H.L., Zhang, Q.C., and Wang, F., 2013: Analysis of a long-lasting haze episode in Nanjing, China. Atmos. Res. 120-121, 78-87.

Kerminen, V.M., Hillamo, R., Teinila, K., Pakkanen, T., Allegrini, I., and Sparapani, R., 2001: Ion balances of size-resolved tropospheric aerosol samples: implications for the acidity and atmospheric processing of aerosols. Atmos. Environ. 35(31), 5255-5265.

Koe, L.C.C., Jr, A.F.A., and McGregor, J.L., 2001: Investigating the haze transport from 1997 biomass burning in Southeast Asia: its impact upon Singapore. Atmos. Environ. 35(15), 2723-2734.

Lam, S.H.M., Saunders, S.M., Guo, H., Ling, Z.H., Jiang, F., Wang, X.M., and Wang, T.J., 2013: Modelling VOC source impacts on high ozone episode days observed at a mountain summit in Hong Kong under the influence of mountain-valley breezes. Atmos. Environ. 81, 166-176.

Lee, E., Chan, C.K., and Paatero, P., 1999: Application of positive matrix factorization in source apportionment of particulate pollutants in Hong Kong. Atmos. Environ. 33, 3201-3212.

Lin, Y.C., Cheng, M.T., Lin, W.H., Lan, Y.Y., and Tsuang, B.J., 2010: Causes of the elevated nitrated aerosol levels during episodic days in Taichung urban area, Taiwan. Atmos. Environ. 44, 1632-1640.

Ling, Z.H., Guo, H., Lam, S.H.M., Saunders, S.M., and Wang, T., 2014: Atmospheric photochemical reactivity and ozone production at two sites in Hong Kong: Application of a master chemical mechanism–photochemical box model. J. Geophys. Res. Atmos. 119, 10567-10582.

737 Liu, Y.J., Zhang, T.T., Liu, Q.Y., Zhang, R.J., Sun, Z.Q., and Zhang, M.G., 2014: Seasonal

738 variation of physical and chemical properties in TSP, PM_{10} and $PM_{2.5}$ at a roadside site in

739 Beijing and their influence on atmospheric visibility. Aerosol Air Qual. Res. 14, 954-969.

740 Liu, Z.R., Hu, B., Wang, L.L., Wu, F.K., Gao, W.K., and Wang, Y.S., 2015: Seasonal and diurnal

741 variation in particulate matter (PM_{10} and $PM_{2.5}$) at an urban site of Beijing: analyses from a 9-

742 year study. Environ. Sci. Pollut. Res. 22, 627-642.

743 Lyu, X.P., Chen, N., Guo, H., Zhang, W.H., Wang, N., Wang, Y., and Liu, M., 2016: Ambient

744 volatile organic compounds and their effect on ozone production in Wuhan, central China. Sci.

745 Total Environ. 541, 200-209.

746 Lyu, X.P., Ling, Z.H., Guo, H., Saunders, S.M., Lam, S.H.M., Wang, N., Wang, Y., Liu, M., and

747 Wang, T., 2015 (b): Re-examination of C_1–C_5 alkyl nitrates in Hong Kong using an

748 observation-based model. Atmos. Environ. 120, 28-37.

749 Lyu, X.P., Wang, Z.W., Cheng, H.R., Zhang, F., Zhang, G., Wang, X.M., Ling, Z.H., Wang, N.,

750 2015 (a): Chemical characteristics of submicron particulates ($PM_{1.0}$) in Wuhan, Central China.

751 Atmos. Res. 161-162, 169-178.

752 Nemesure, S., Wagener, R., and Schwartz, S.E., 1995: Direct shortwave forcing of climate by the

753 anthropogenic sulfate aerosol: sensitivity to particle size, composition, and relative humidity. J.

754 Geophys. Res. 100, 26105-26116.

755 Nriagu, J.O., and Pacyna, J.M., 1988: Quantitative assessment of worldwide contamination of air,

756 water and soils by trace metals. Nature 333, 134-139.

757 Oanh, N.T.K., and Leelasakultum, K., 2011: Analysis of meteorology and emission in haze

758 episode prevalence over mountain-bounded region for early warning. Sci. Total Environ.

759 409(11), 2261-2271.

760 Paatero, P., and Tapper, U., 1994: Positive matrix factorization: A non-negative factor model with

761 optimal utilization of error estimates of data values. Environmetrics 5, 111-126.

762 Paatero, P., 1997: Least squares formulation of robust non-negative factor analysis. Chemom.

763 Intell. Lab. Sys. 37, 23-35.

764 Pathak, R.K., Wang, T., and Wu, W.S., 2011: Nighttime enhancement of $PM_{2.5}$ nitrate in

765 ammonia-poor atmospheric conditions in Beijing and Shanghai: Plausible contributions of

766 heterogeneous hydrolysis of N_2O_5 and HNO_3 partitioning. Atmos. Environ. 45, 1183-1191.

767 Querol, X., Alastuey, A., Viana, M.M., Rodriguez, S., Artinano, B., Salvador, P., Garcia do

Santos, S., Fernandez Patier, R., Ruiz, C.R., de la Rosa, J., Sanchez de la Campa, A., Menendez, M., and Gil, J.I., 2004: Speciation and origin of PM_{10} and $PM_{2.5}$ in Spain. J. Aerosol Sci. 35, 1151-1172.

Ramanathan, V., Crutzen, P.J., Kiehl, J.T., and Rosenfeld, D., 2001: Aerosol, climate and the hydrological cycle. Science 294, 2119-2124.

Saarikoski, S., Sillanpaa, M., Sofiev, M., Timonen, H., Saarnio, K., Teinila, K., Karppinen, A., Kukkonen, J., and Hillamo, R., 2007: Chemical composition of aerosols during a major biomass burning episode over northern Europe in spring 2006: Experimental and modelling assessments. Atmos. Environ. 41, 3577-3589.

Seinfeld, J.H., and Pandis, S.N., 1998: Atmospheric chemistry and physics from air pollution to climate change. New York: Wiley, p. 528.

Shen, G.F., Yuan, S.Y., Xie, Y.N., Xia, S.J., Li, L., Yao, Y.K., Qiao, Y.Z., Zhang, J., Zhao, Q.Y., Ding, A.J., Li, B., and Wu, H.S., 2014: Ambient levels and temporal variations of $PM_{2.5}$ and PM_{10} at a residential site in the mega-city, Nanjing, in the western Yangtze River Delta, China. J. Environ. Sci. Health: Part A 49(2), 171-178.

Shen, Z.X., Cao, J.J., Liu, S.X., Zhu, C.S., Wang, X., Zhang, T., Xu, H.M., and Hu, T.F., 2011: Chemical compositions of PM_{10} and $PM_{2.5}$ collected at ground level and 100 meters during a strong winter-time pollution episode in Xi'an, China. J Air Waste Manage. Assoc. 61(11), 1150-1159.

Simoneit, B.R.T., 2002: Biomass burning-a review of organic tracers for smoke from incomplete combustion. Appl. Geochem. 17(3), 129-162.

Song, S., Wu, Y., Jiang, J., Yang, L., Cheng, Y., and Hao, J., 2012. Chemical characteristics of size-resolved $PM_{2.5}$ at a roadside environment in Beijing, China. Environ. Pollut. 161, 215-221.

Takekawa, H., Minoura, H., and Yamazaki, S., 2003. Temperature dependence of secondary organic aerosol formation by photo-oxidation of hydrocarbons. Atmos. Environ. 37, 3413-3424.

Tang, I.N., and Munkelwitz, H.R., 1993: Compositions and temperature dependence of the deliquescence properties of hygroscopic aerosols. Atmos. Environ. 27, 467-473.

Theodosi, C., Grivas, G., Zarmpas, P., Chaloulakou, A., and Mihalopoulos, N., 2011: Mass and chemical composition of size-segregated aerosols (PM_1, $PM_{2.5}$, PM_{10}) over Athens, Greece: local versus regional sources. Atmos. Chem. Phys. 11, 11895-1191.

Wang, H., Tan, S.C., Wang, Y., Jiang, C., Shi, G.Y., Zhang, M.X., and Che, H.Z., 2014 (a): A multisource observation study of the severe prolonged regional haze episode over eastern China in January 2013. Atmos. Environ. 89, 807-815.

Wang, H., Xu, J.Y., Zhang, M., Yang, Y.Q., Shen, X.J., Wang, Y.Q., Chen, D., and Guo, J.P., 2014 (b): A study of the meteorological causes of a prolonged and severe haze episode in January 2013 over central-eastern China. Atmos. Environ. 98, 146-157.

Wang, H.L., Lou, S.R., Huang, C., Qiao, L.P., Tang, X.B., Chen, C.H., Zeng, L.M., Wang, Q., Zhou, M., Lu, S.H., and Yu, X.N., 2014: Source profiles of volatile organic compounds from biomass burning in Yangtze River Delta, China. Aerosol Air Qual. Res. 14, 818-828.

Wang, J., Hu, Z.M., Chen, Y.Y., Chen, Z.L., and Xu, S.Y., 2013: Contamination characteristics and possible sources of PM_{10} and $PM_{2.5}$ in different functional areas of Shanghai, China. Atmos. Environ. 68, 221-229.

Wang, P., Cao, J.J., Tie, X.X., Wang, G.H., Li, G.H., Hu, T.F., Wu, Y.T., Xu, Y.S., Xu, G.D., Zhao, Y.Z., Ding, W.C., Liu, H.K., Huang, R.J., and Zhan, C.L., 2015: Impact of meteorological parameters and gaseous pollutants on $PM_{2.5}$ and PM_{10} mass concentrations during 2010 in Xi'an, China. Aerosol Air Qual. Res. 15, 1844-1854.

Wang, S.X., Zhang, L., Li, G.H., Wu, Y., Hao, J.M., Pirrone, N., Sprovieri, F., and Ancora, M.P., 2010. Mercury emission and speciation of coal-fired power plants in China. Atmos. Chem. Phys. 10, 1183-1192.

Wang, Y.X., Zhang, Q.Q., Jiang, J.K., Zhou, W., Wang, B.Y., He, K.B., Duan, F.K., Zhang, Q., Philip, S., and Xie, Y.Y., 2014: Enhanced sulfate formation during China's severe winter haze episode in January 2013 missing from current models. J. Geophys. Res. 119, 10425-10440.

White, W.H., and Roberts, P.T., 1977: On the nature and origins of visibility-reducing aerosols in the Los Angeles air basin. Atmos. Environ. 11(9), 803-812.

Wuhan Environmental Bulletin, 2014, accessible at http://www.whepb.gov.cn/zwGkhjtj/16240.jhtml.

Yang, L., Cheng, S., Wang, X., Nie, W., Xu, P., Gao, X., Yuan, C., and Wang, W., 2013. Source identification and health impact of $PM_{2.5}$ in a heavily polluted urban atmosphere in China. Atmos. Environ. 75, 265-269.

Yang, L.X., Zhou, X.H., Wang, Z., Zhou, Y., Cheng, S.H., Xu, P.J., Gao, X.M., Nie, W., Wang, X.F., and Wang, W.X., 2012: Airborne fine particulate pollution in Jinan, China:

Concentrations, chemical compositions and influence on visibility impairment. Atmos. Environ. 55, 506-514.

Yao, X.H., Chan, C.K., Fang, M., Candle, S., Chan, T., Mulawa, P., He, K.B., and Ye, B., 2002: The water-soluble ionic composition of $PM_{2.5}$ in Shanghai and Beijing, China. Atmos. Environ. 36(26), 4223-4234.

Ye, B., Ji, X., Yang, H., Yao, X., Chan, C.K., Cadle, S.H., Chan, T., and Mulawa, P.A., 2003. Concentration and chemical composition of $PM_{2.5}$ in Shanghai for a 1-year period. Atmos. Environ. 37, 499-510.

Zhang, F., Cheng, H.R., Wang, Z.W., Lv, X.P., Zhu, Z.M., Zhang, G., and Wang, X.M., 2014: Fine particles ($PM_{2.5}$) at a CAWNET background site in Central China: Chemical compositions, seasonal variations and regional pollution events. Atmos. Environ. 86, 193-202.

Zhang, G.H., Bi, X.H., Chan, L.Y., Wang, X.M., Sheng, G.Y., and Fu, J.M., 2013: Size-segregated chemical characteristics of aerosol during haze in an urban area of the Pearl River Delta region, China. Urban Climate 4, 74-84.

Zhang, Q., Jimenez, J.L., Worsnop, D.R., Canagaratna, M., 2007: A case study of urban particle acidity and its influence on secondary organic aerosol. Environ. Sci. Technol. 41(9), 3213-3219.

Zhang, X.Y., Wang, Y.Q., Niu, T., Zhang, X.C., Gong, S.L., Zhang, Y.M., and Sun, J.Y., 2012: Atmospheric aerosol compositions in China: Spatial/temporal variability, chemical signature, regional haze distribution and comparisons with global aerosols. Atmos. Chem. Phys. 12, 779-799.

Zhang, Y.Y., Obrist, D., Zielinska, B., and Gertler, A., 2013: Particulate emissions from different types of biomass burning. Atmos. Environ. 72, 27-35.

Zheng, M., Salmon, L.G., Schauer, J.J., Zeng, L.M., Kiang, C.S., Zhang, Y.H., and Cass, G.R., 2005: Seasonal trends in $PM_{2.5}$ source contributions in Beijing, China. Atmos. Environ. 39(22), 3967-3976.